DESIGN AND ECONOMIC ANALYSIS OF NANOFLUID BASED PHOTOVOLTAIC THERMAL SYSTEM WITH THERMAL STORAGE

BY

MUHAMMAD OWAIS LARI

A Thesis Presented to the
DEANSHIP OF GRADUATE STUDIES

KING FAHD UNIVERSITY OF PETROLEUM & MINERALS

DHAHRAN, SAUDI ARABIA

In Partial Fulfillment of the
Requirements for the Degree of

MASTER OF SCIENCE

In

MECHANICAL ENGINEERING

APRIL 2017

KING FAHD UNIVERSITY OF PETROLEUM & MINERALS

DHAHRAN- 31261, SAUDI ARABIA

DEANSHIP OF GRADUATE STUDIES

This thesis, written by **Muhammad Owais Lari** under the direction his thesis advisor and approved by his thesis committee, has been presented and accepted by the Dean of Graduate Studies, in partial fulfillment of the requirements for the degree of **MASTER OF SCIENCE IN MECHANICAL ENGINEERING**

Dr. Ahmet Ziyaettin Sahin
(Advisor)

Dr. Zuhair M. Gasem
Department Chairman

Dr. Bekir Sami Yilbas
(Member)

Dr. Salam A. Zummo
Dean of Graduate Studies

Dr. Fahad Abdulaziz Alsulaiman
(Member)

26/9/17

Date 02/05/2017

This work is dedicated to my beloved family.

ACKNOWLEDGMENTS

First, I praise and thank ALLAH (S.W.T.) THE MOST GRACIOUS, THE MOST MERCIFUL for HIS KINDNESS and the innumerable favors which HE has bestowed upon me throughout my life.

I would love to express my gratitude towards my family: My mother for her unconditional love and belief in me which gave me confidence in my abilities, my father for his unwavering support which gave me a sense of complete security and my sisters for inspiring and encouraging me.

I would like to express my special gratitude to my advisor, Dr. Ahmet Ziyaettin Sahin for his guidance and help in completing this endeavor.

I would also like to acknowledge my committee members: Dr. Bekir Sami Yilbas and Dr. Fahad Abdulaziz Alsulaiman who graciously agreed to be on my committee.

Finally, I would like to thank the Dean and Faculty of Mechanical Engineering Department and the Centre of Engineering Research, KFUPM.

May Allah, bless you all.

TABLE OF CONTENTS

LIST OF TABLES

LIST OF FIGURES

LIST OF ABBREVIATIONS

a	ideality factor
A_c	Collector Area, m^2
Ag	Silver
c_p	Specific heat capacity, J/kg.K
Δp	Pressure drop, Pa
d	Diameter, m
D	Annual rate of performance degradation, %
E	Electrical energy saved, kW.hr
ε	Emittance
Ex	Rate of exergy, W
E_g	Band gap energy, J
F_R	Collector heat removal factor
f	Friction factor
g	Gravitational constant, m/s
G_{sc}	Solar constant, W/m^2
h	heat transfer coefficient, $W/m^2{}^\circ C$
I	Current, A / Incident radiation, W/m^2
I_{ET}	Extra-terrestrial radiation, W/m^2
I_L	Light generated current, A

I_o	Diode reverse saturation current, A
I_T	Total radiation, W/m^2
i	rate, %
k	Thermal conductivity, W/m.K
k_t	Clearness index
K_L	Minor head loss coefficient
L	Length, m
n	representative day of the month
N_s	Number of cells
n_g	Refractive index of glass
OAK^+	Potassium oleate
P	Electrical power, W
ρ_g	Ground reflectance
φ_{nf}	nanoparticle volumetric concentration, %vol
R_b	Ratio of radiation on tilted surface to that on horizontal surface
R_s	Series resistance, Ω
R_{sh}	Shunt resistance, Ω
S	Absorbed radiation, W/m^2
T	Temperature, ˚C
T_c	Cell Temperature, K
T_{cell}	Cell Temperature, ˚C
U	Heat loss coefficient, W/m^2˚C

Q	Thermal power, W
V	Voltage, V
W	Width, m

Greek letters

α	PV absorptance
β	Collector tilt angle, ˚
δ	Declination angle, ˚ / Thickness, m
η	Efficiency
μ	Absolute viscosity, kg/s.m / Temperature coefficient, V˚C/ A˚C
ω	Average hour angle, ˚
ϕ	Latitude, ˚N
ρ	Density, kg/m^3
σ	Stefan-Boltzmann constant, W/m^2 K^4
τ	Transmittance
θ_1	Incidence angle, ˚

Subscripts

a	ambient
b	beam / bottom
coll	collector
cw	cold domestic water
d	diffuse / discount
e	edge / inflation

ec	inflation of domestic electricity price
f	base fluid
fluid	collector fluid
g	glass/ground
h	thermal system
hxg	heat exchanger
i	inlet
Isc	short circuit current
L	electrical system
mp	maximum power
n	nanoparticle
np	lifetime of system, years
o	outlet
ref	reference conditions
PV	PV panel
t	top
TB	thermal battery
Voc	open citcuit voltage
w	domestic water
Y	year

Abbreviations

AM	Air mass
ALCC	Annualized life cycle cost, $
BIPVT	Building integrated photovoltaic thermal
COE	Cost of energy, $/kW.hr
CPBT	Cost payback time, years
CF	Cash flow, $
CRF	Capital recovery factor
DCF	Discounted cash flow, $
EC	Electricity cost saved, $
FPSC	Flat plate solar collector
IC	Investment cost, $
LCC	Life cycle cost, $
MC	Maintenance cost, $
PV	Photovoltaic
PVT	Photovoltaic thermal
PCM	Phase change material
RC	Replacement cost, $
STC	Standard test conditions
WS	Wind speed, m/s

ABSTRACT

Full Name : Muhammad Owais Lari

Thesis Title : Design and economic analysis of nanofluid based photovoltaic thermal (PVT) system with thermal storage

Major Field : Mechanical Engineering

Date of Degree : May 2017

This thesis is focused on the design optimization of a hybrid solar photovoltaic/thermal (PVT) system suitable to meet the electrical and hot water load fluctuations of a residential building for the climate of Dhahran, Saudi Arabia. A PVT collector is a hybrid device which cools the solar photovoltaic (PV) panel through a fluid, thereby increasing the electrical yield and life of solar panel, while simultaneously recovering the excess thermal energy in the form of hot fluid. Due to their superior thermal properties, the use of nanofluids as coolant in PVT systems have become increasingly common. Also, addition of a suitable thermal storage device to the system is necessary to address the mismatch in the thermal energy supply and demand profiles. In this thesis, optimum collector design is selected through simulations on CFD software FLUENT, after which daily and yearly performance evaluation of the system is analytically performed through Engineering Equation Solver (EES) software. PVT system's performance, for the case of both water and nanofluid, is compared with that of a stand-alone PV system. Furthermore, the design and performance evaluation of a novel PVT system integrated with a Phase Change Material (PCM)-thermal storage is presented along with an economic feasibility study.

ملخص الرسالة

الاسم الكامل: محمد أويس لاري

عنوان الرسالة: صميم والتحليل الاقتصادي من نظام الطاقة الشمسية الضوئية القائمة على النانو مع التخزين الحراري

التخصص: مهندس ميكانيكى

تاريخ الدرجة العلمية: شعبان ١٤٣٨

هذه الرسالة مركزة على التصميم الأمثل لنظام الطاقة الشمسية الضوئية / الحرارية الهجين (PVT) المناسب لتلبية تقلبات الحمل الكهربائي والماء الساخن للمبنى السكني لمناخ الظهران بالمملكة العربية السعودية. إن جهاز التجميع PVT هو جهاز هجين يبرد لوحة الطاقة الشمسية الكهروضوئية باستخدام سائل، مما يزيد من العائد الكهربائي ومن عمر الألواح الشمسية، بينما في الوقت ذاته يستعيد الطاقة الحرارية الزائدة في على شكل سائل ساخن. نظرا لخصائصها الحرارية المتفوقة، أصبح استخدام سوائل النانو المبردة في أنظمة PVT شائعة على نحو متزايد. إضافة إلى ذلك، من الضروري إضافة جهاز تخزين حراري مناسب إلى النظام لمعالجة عدم التطابق في ملامح العرض والطلب للطاقة الحرارية. في هذه الأطروحة، يتم اختيار تصميم يتم اختيار التصميم الأمثل من خلال محاكاة على برنامج FLUENT، وبعد ذلك يتم إجراء تقييم الأداء اليومي والسنوي من النظام تحليليا من خلال برنامج حل المعادلات الهندسية (EES). يتم مقارنة أداء النظام PVT، في حالة كل من المياه وسائل النانو، مع النظام الكهروضوئي المستقل. وعلاوة على ذلك، يتم عرض تصميم وتقييم أداء نظام PVT جديد متكامل مع تخزين حراري لمادة تتغير حالتها (PCM) - جنبا إلى جنب مع دراسة الجدوى الاقتصادية.

CHAPTER 1

INTRODUCTION

1.1 Background

Due to the increasing dependence on technology all over the world, energy is fast becoming the most crucial requirement for society. The continuous increase in world's population coupled with the spread of modernization has resulted in a two-fold increase in the worldwide demand for energy during the first half of the twenty-first century, and this demand is expected to triple by the end of this century. Fossil fuels were the most convenient source of energy; however, the reserves of fossil fuels are neither vast, nor renewable. Furthermore, decades worth of unrestrained use of fossil fuel for energy meant that exorbitant amounts of pollutants have been dumped into the atmosphere. This relentless pollution of the environment was the major reason for global warming and has resulted in the current shift in global climate. Climate change is one of the most formidable enormities being faced by the modern world.

Increasing energy consumption and the depletion of fossil fuel reserves, along with the dangerous phenomena of climate change has led to a growing awareness of renewable energy resources all over the world. Among the different types of renewable energy resources, solar provide an attractive alternative especially for areas with high average annual solar radiation. Solar energy is fast becoming one of the most important sources of renewable energy because it is free of cost, it is abundant, it is easily available and it produces zero atmospheric pollutants or emissions. Solar energy can be directly converted

to either electrical or thermal energy. The conversion of solar energy to thermal energy and further conversion to electricity has received considerable attention. Solar thermal collectors which convert solar to thermal energy are one of the most elementary solar devices and a well-designed solar thermal collector can convert a major portion (above 50 %) of incident solar energy to thermal energy. A photovoltaic (PV) cell, more commonly known as a solar cell is an electrical device which directly converts sunlight into electrical energy through the photovoltaic effect.

PV modules, which are a collection of PV cells, are becoming increasingly common as a source of electrical energy at both domestic and industrial levels. PV modules are emission-free, require little maintenance, do not burden the consumer with fuel costs and they work noiselessly with no toxic residues or unwanted waste, such as radioactive materials, which is why they have been selected as the topic of focus in this study.

1.2 PVT system and use of nanofluid

The most widely available PV modules are made of crystalline silicon and can only convert a small portion (4-17%) of incident solar energy to electrical energy. Which means that more than 80 % of the incident energy remains unconverted and serves only to heat up the PV module. Hence, exposing PV modules to sunlight together with high ambient temperatures and low wind speeds will result in extreme rises in solar cell working temperatures (sometimes as much as 50˚C) above the ambient temperature.

Increases in solar cell temperatures leads to a loss in the electrical yield of solar cells and can even result in permanent structural damage if thermal stresses remain in the module

for a prolonged period. A PV module can be cooled by attaching it to the top of a solar thermal collector. The fluid circulating through the collector will remove the excess heat from the PV module lowering its temperature. Such a hybrid device is called a photovoltaic thermal (PVT) collector and it supplies both electricity and heat in the form of hot fluid. A PVT collector has higher energy yield per unit area than either PV or solar collector as the electrical efficiency of a PVT-integrated PV panel is higher than that of a standalone PV system. Since a PVT system can provide both electrical and thermal energy simultaneously it can fulfill part of the electricity and hot water requirements of buildings, such as hospitals, schools, hotels, and houses.

The fluid used to cool the PV cells has a significant impact on the overall performance of PVT system. Earlier designs of PVT system used either air or water as coolant. However low thermal conductivity of fluids used in solar systems such as water or ethylene glycol has been one of the primary limitations to the efficiency improvement of such systems. One of the techniques used to overcome this limitation is the use of nanofluids as the heat transfer fluids in solar collectors. Nanofluids consist of nano-sized particles suspended in base fluids such as water or oil. Owing to their small size the nanoparticles always remain in suspension and even the introduction of a small fraction of nanoparticles greatly enhances the thermal properties of base fluids. The addition of silver (Ag) nanoparticles to the water have resulted in high-thermal conductivity nanofluids [1], consequently, silver/water nanofluids have been successfully implemented in experimental studies for both FPSC [2] and PVT systems [3].

1.3 Importance of latent thermal storage in PVT systems

The intermittent nature of solar energy makes it difficult to follow the thermal load of a building, especially if the thermal load profile contains features such as negligible load in daylight hours and peak loads in the early morning and late afternoon. In the absence of a thermal storage device, this mismatch in thermal energy supply and demand would result in most of the heat remaining in the system. This heat must be removed or else it will remain in the system and heat up the PV module which would deteriorate the PV panel performance.

The advantage of the use of latent storage over sensible storage, in this case, is the provision of control over the inlet collector fluid temperature for subsequent hours. This is due to the isothermal nature of phase change material which does not undergo a change in temperature when the thermal battery is charged (addition of heat). The provision of control over the collector inlet fluid temperature allows for control over the electrical performance of the system because low collector inlet fluid temperatures result in low cell temperatures which lead to improved electrical performance. Figure 1.1 shows that in a thermal battery-assisted PVT system, collector inlet fluid temperature strongly depends on the phase change temperature of the latent heat storage material. Hence the lower the phase change temperature of storage material, the better the electrical performance of the system.

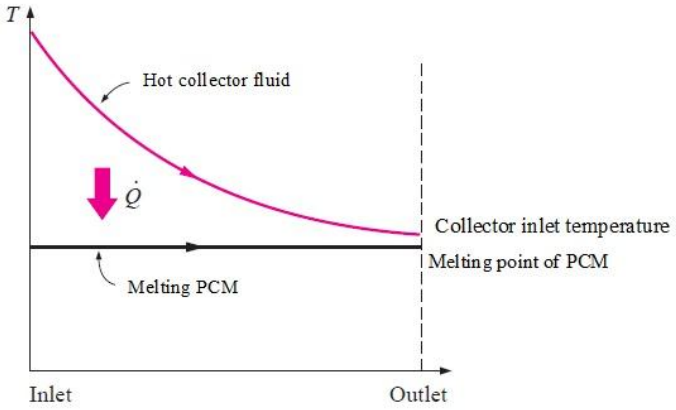

Figure 1.1 Variation of collector fluid temperature in thermal battery as PCM melts

However, the major limitation of this design is exhibited during the discharging phase of the thermal battery. Since temperature difference is the driving force for heat transfer, thus to extract heat from the PCM, the heat transfer fluid inlet temperature should be well below the melting point of PCM and the maximum temperature which the heat transfer fluid can be heated to will be below the phase change temperature of storage material. This heat transfer fluid is responsible for heating water for domestic use through a heat exchanger. Hence, the lower the phase change temperature of storage material, the lower the temperature of the heated domestic water and the worse the thermal performance of the system. Since domestic water must be heated to a temperature of at least 50 ˚C, lower phase change temperature of storage material would necessitate the increased use of auxiliary electric water heater to heat domestic water.

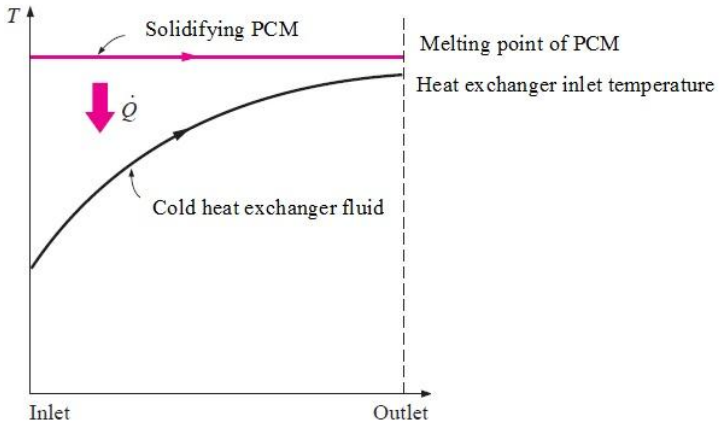

Figure 1.2 Variation of heat exchanger fluid temperature in thermal battery as PCM solidifies

Thus, the major limitation of this design is the phase change temperature of storage material, since lower phase change temperatures would improve the electrical performance but worsen the thermal performance of the system. A compromise can only be developed based on the priorities of the designer. Since the main motivation for the development of PVT technology was the elevated solar cell temperatures and the subsequent loss in the electrical performance of PV panel, high phase change temperatures of storage material would not make sense.

In this study, cold domestic water is available at a maximum temperature of 25 ˚C in summer months but the temperatures are lower in winter months (as low as 12.5 ˚C). The melting point of PCM must be higher than 25 ˚C so that heat can be extracted from the PCM in summer months. A PCM having a melting point of 28 ˚C has been chosen to restrict the rise in solar cell temperature. Hence domestic water will gain very little heat from the system in summer months, but system's performance will improve in winter months.

1.4 Research objectives

The absence of a PVT system integrated with a thermal storage, suitable for a typical residential thermal load profile has been noted in the existing literature. The inclusion of an efficient thermal storage is necessary to take care of the mismatch in temporal profiles of thermal energy supply and demand. The aim of this study is to design a nanofluid-based PVT system consisting of an efficient thermal collector and a thermal storage to cover part of the electrical and thermal load of a residential building for the climate of Saudi Arabia. Hence, the objectives of this study are:

- Design optimization of the PVT-integrated thermal collector through CFD
- Design and sizing of a nanofluid-based PVT system to cover a portion of the electrical load for a residential building in Saudi Arabia
- Hourly and monthly performance evaluation of the nanofluid-based PVT system for the meteorological conditions of Dhahran, Saudi Arabia
- Study the effect of introducing a PCM-based thermal battery into the system
- Life-cycle cost analysis of the proposed system for the economic conditions of Saudi Arabia

CHAPTER 2

LITERATURE REVIEW

2.1 Energy demand and the potential for solar energy in Saudi Arabia

Increasing electricity consumption and depleting fossil fuel reserves, along with adverse environmental effects have led to a growing awareness of renewable energy resources in Saudi Arabia. Saudi Arabia is the fastest growing electricity consumer in the Middle East, and it consumes three times more electricity than the world average [4]. The per capita electricity consumption, which grew by nine percent in 2012 relative to the previous year, is increasing year after year [4]. The per capita electricity consumption was 6,980.92 kWh per person in 2014 and the total power consumption in the Kingdom is expected to reach 90,000 megawatts within 10 years [5]. In 2008, the residential sector accounted for about 53% of total energy consumption amounting to 181.1 billion kW.hr [6].

Electricity in the Kingdom is generated mostly through thermal power plants which consume fossil fuels. Over the period of 2000 to 2007, consumption of heavy fuel oil, in power plants, increased at an average annual rate of about 15.7 %, with natural gas consumption, increasing at an average annual growth rate of 10.4 % [6]. Furthermore, the Kingdom's population grew sevenfold from 1960 to 2010, and petroleum prices in the Kingdom are subsidized and cost less than equivalent quantities of bottled water. Heavy domestic consumption and exportation have accelerated the depletion rate of the Kingdom's petroleum reserves. With over 80% of current GDP coming from oil exports, the Saudi government is eager to find a solution to growing domestic energy demand.

Since the Kingdom relies heavily on oil for electricity production, measuring solar grid parity in Saudi Arabia is best done by comparing the cost of solar electricity generation with the opportunity cost of burning oil for electricity rather than export. According to Clear Sky Advisors' analysis, solar energy in Saudi Arabia is currently cost competitive with oil fired power plants [7]. The analysis states that with currently available technologies and cost structures, large-scale solar PV costs less than 0.15 $/kW.hr, while the opportunity cost of burning oil for electricity costs the Kingdom between 0.127 to 0.174 $/kW.hr [7].

Saudi Arabia is also conveniently located in the Sun Belt to take advantage of solar energy. Average solar radiation in Saudi Arabia varies between a maximum of 7.004 kWh/m^2 at Bisha and a minimum of 4.479 kWh/m^2 at Tabuk. In addition, the costs of solar PV are expected to decrease further as the industry within Saudi Arabia develops, making solar power even more attractive within the region.

2.2 Effect of temperature on photovoltaic cells

The electrical performance of a PV cell is sensitive to changes in temperature. Most PV cells are manufactured using semiconductor materials such as crystalline silicon and the flow of PV current across the cell requires electrons (charge carriers) in the conduction band of an atom. An electron must acquire sufficient energy to overcome the band gap energy E_g and jump from the valence to the conduction band. Since band gap energy, E_g, and temperature is linearly related [8]

$$E_g\,(T_c) = E_g\,(300\ K) + \frac{dE_g}{dT_c}\,(T_c - 300\ K) \qquad (2.1)$$

The band gap energy decreases with increasing temperature, hence the concentration of charge carriers decreases with increasing temperature [9]. Incident light strikes a PV cell, penetrates through it and generates charge carriers. Higher cell temperatures reduce the depth of light penetration and also increase thermal lattice vibrations which obstruct the charge carriers mobility [9].

The Current-Voltage curve of a PV cell changes with temperature. According to Van Dyk, for crystalline silicon, the short-circuit current increases with increasing temperature at a rate of 0.06 %/°C [10] and the open-circuit voltage decreases with increasing temperature at a rate of 0.4 %/°C[10].

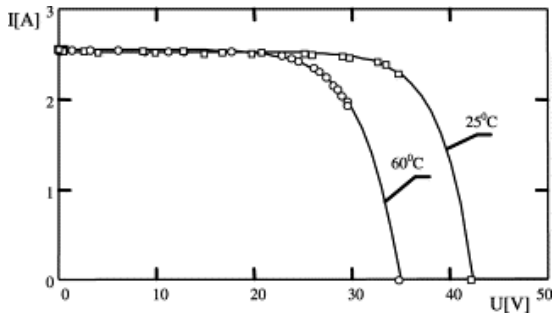

Figure 2.1 Changes in PV Power-Voltage curve with cell temperatures at 28°C, 40°C, 60°C, 80°C

Results of Van Dyk [10] indicate that the maximum PV power output decreases with increasing temperature at a rate of 0.4-0.5 %/°C.

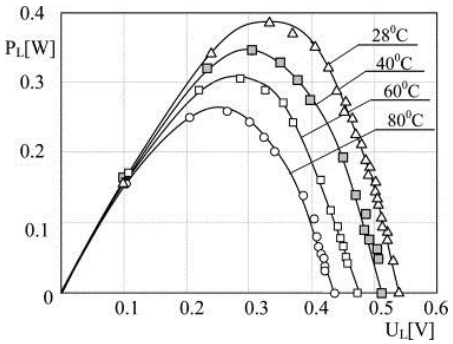

Figure 2.2 Changes in PV Power-Voltage curve with cell temperatures at 28°C, 40°C, 60°C, 80°C

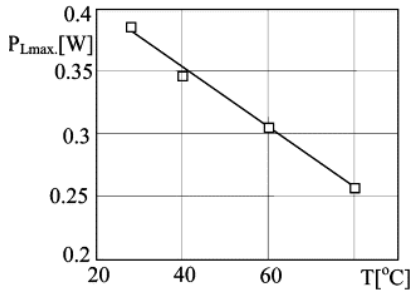

Figure 2.3 Changes in PV maximum Power output with cell temperature

Effect of temperature on a PV cell varies with the cell's crystalline structure as well as its composition. Experimental studies report a drop in the maximum power of 0.446%/°C [11] to 0.48%/°C [10] for a mono-crystalline cell, 0.387%/°C [11] to 0.46%/°C for a polycrystalline cell[10] , 0.42%/°C for Edge-defined Film-fed Growth (EFG) cell [10]. Second-generation thin-film solar cells are more resistant to changes in temperature with a maximum power drop of 0.234%/°C [11] to 0.25 %/°C [12] for amorphous silicon, 0.172 %/°C [11] for Cadmium Tellurium (CdTe), only 0.08%/°K for GaAs [13] and 0.078 mW/cm^2.°C for Copper Indium Gallium Selenide (CIGS) [14]. Second-generation solar cells are seldom used since either they have low efficiencies (amorphous silicon) or are too expensive (CIGS and GaAs) hence are only suitable for applications such as spacecraft or space-based solar power generation. Multi-junction solar cells are mostly used in the case of concentrated solar power [15,16], hence they are not discussed. Polycrystalline cells have lower efficiencies than mono-crystalline cells but are simpler to produce with lower manufacturing costs and less wastage of silicon. This study uses a polycrystalline photovoltaic module along with the five-parameter model described by De Soto et. al [17] to predict the module's electrical performance.

2.3 Design of PVT collector

In any type of solar cell, the electrical performance of the cell deteriorates with increase in temperature. Since less than 50% of the absorbed solar radiation can be converted to electricity, it is important to remove the remaining energy or it will lead to extreme cell temperatures. Photovoltaic thermal collectors (PVT) combine photovoltaic modules with solar thermal collectors in such a way that it cools the solar cells and improves their performance while simultaneously increasing the energy yield per unit panel area by providing thermal energy in the form of a hot fluid, which may be used for various purposes. Over the years many different types of design have been suggested ranging from flat-plate to concentrating collectors, forced convection (active) to free convection (passive) systems, glazed or unglazed panels, air or water-based collectors, monocrystalline/polycrystalline or any other type of PV panel, single-pass or double-pass channel and channel above PV or below PV. Figure 4 shows the main features of a PVT collector.

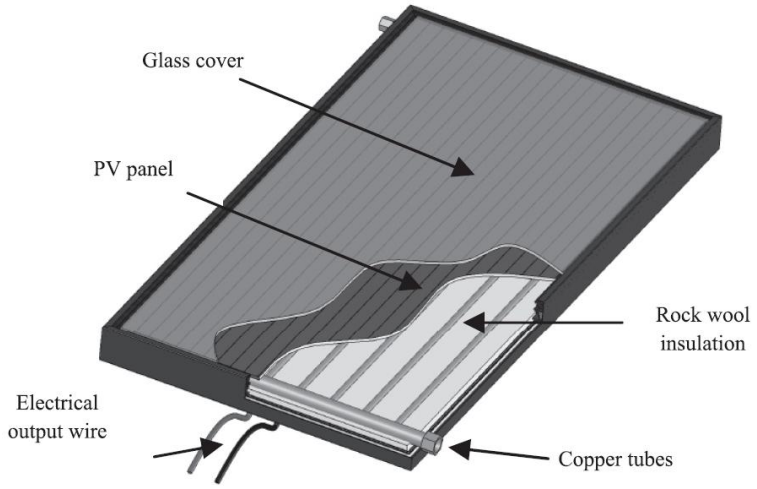

Figure 2.4 Main features of a PVT collector

In a concentrating PVT system, sunlight is focused via reflectors or lenses onto the PVT system to increase the radiation flux to the system. However, to exploit the extra energy input high-efficiency solar cells (second-generation or third-generation solar cells) are required, along with complex sun tracking mechanism which increases the expenses and complexity of the system [18]. Furthermore, concentrating systems which use lenses to focus sunlight cannot be used in areas which receive scattered sunlight and hence are ineffective in clear weather conditions [19]. An experimental comparison was performed between a Flat plate PVT system and Compound Parabolic Concentrating PVT system [20] for fluid inlet temperatures ranging from 23˚C to 40˚C; results show that thermal efficiency is higher for flat plate systems as compared to concentrating systems due to a lower heat loss coefficient for flat plate systems. According to PVT roadmap [21], the major market potential for PVT system lie in the domestic sector, hence PVT system should be economically viable for the domestic market. In this study, a flat plate PVT system is used for domestic hot water applications.

The use of both free and forced convection in cooling PV modules has been studied. Theoretical [22] and experimental [23] studies have been performed on thermosyphon systems which utilize the natural fluid flow currents set up due to the temperature difference. The main advantage of such passive systems is the absence of an electrical pump to push the fluid along the collector. Since temperature difference provides the driving force for fluids, such passive systems require large temperature difference and are not suitable for low-temperature systems. Additionally, in such systems, the amount of water in the tank also affects the system's performance significantly [22]. Passive systems

offer less control; also forced circulation is better due to higher convective heat transfer coefficients. In this study, forced convection is used to cool the PV module.

Effect of using glass cover (glazed system) on the performance of a PVT system has been extensively studied. Use of a glass cover over the PV cells is important as it protects the sensitive PV cells from environmental factors such as rain, dust, and pollutants. Experimental results [24–26] show that a glass cover together with an air gap over the PV cells increases the thermal efficiency of a system as it reduces the heat loss coefficient, however, this increase in thermal efficiency heats up the absorber and reduces the electrical efficiency of PV cells. Additionally, the presence of glass cover reduces the optical as well as the electrical efficiency of the system since less radiation reaches the PV cells.Most commercially available PV modules have silicon cells sandwiched between a glass cover and a back sheet with no air gap and such a PV module is used in this study as well.

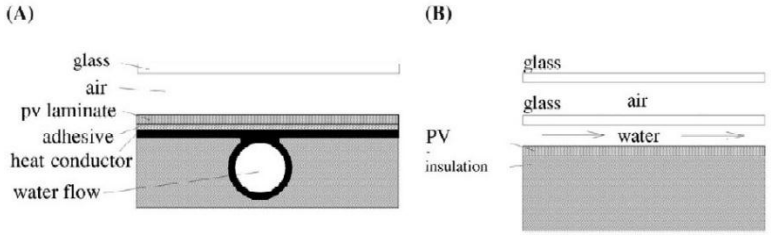

Figure 2.5 Various collector concepts: (A) sheet-and-tube PVT, (B) channel PVT

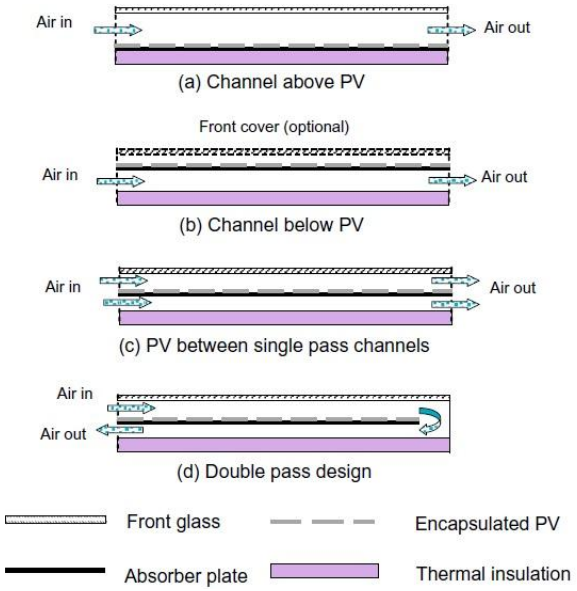

Figure 2.6 Longitudinal cross-section of a few PVT collector designs

Figure 5 shows various PVT collector design concepts. In addition to sheet and tube design, channel collectors have also been manufactured and tested. Channel collectors may be further classified according to flow configurations: single pass channel, double-pass channel, channel above PV or channel below PV as shown in figure 6. Analytical comparison between single pass and double pass PVT systems with air [27] and nanofluid [3] as coolant was performed. Results show superior performance of double pass PVT systems for air but poorer performance for nanofluids as compared to single pass PVT systems. Various experimental studies [28,29] were performed for PVT systems in which water (coolant) was flowing above the PV panel. Analytical calculations [30] show that channel below PV systems have lower PV temperatures and therefore higher electrical efficiencies than channel above PV. As compare to channel PVT systems, sheet and tube PVT systems are simpler to construct and easier to analyze since they rely on well-established technologies and mathematical models and were among the earliest PVT designs. Analytical results [30] showed that the thermal efficiency of sheet and tube design

is only 2% lower than that of the channel below PV design; additionally, the sheet and tube design is easier to manufacture as well. This study uses a sheet and tube single pass design with the collector attached beneath the PV module.

In an attempt to induce uniformity in the temperatures of PV cells along the absorber for sheet and tube PVT systems, many collector configurations have been suggested. In most studies, numerical simulations have been carried out using computational fluid dynamics to study the temperature distributions across PV panel. The two most popular configurations found in the literature are the serpentine collector and the header-riser collector as shown in figure 7.

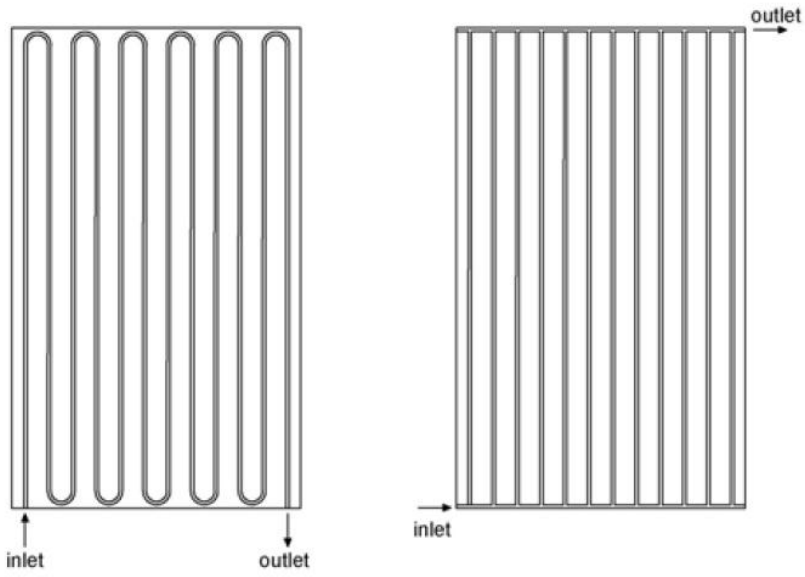

Figure 2.7 Serpentine collector and the Header-riser collector

Indoor experimental testing [25] was performed to compare the performance of PVT systems using serpentine and header-riser collector. Results show that the PVT collector having a serpentine absorber has superior thermal performance as compare to header-riser configuration due to reduced heat loss coefficient. The temperature distribution of the two collectors showed that the temperature of PV cells increased from left to right for the

serpentine collector and from top to bottom for the header-riser collector. Pressure drop is higher in serpentine collector since the fluid has to travel a longer distance as compared to the fluid in header-riser collector. On the other hand, numerical simulation [31] was carried out to determine the effect of the two configurations on the electrical performance of PV panel for four different configurations of PV cells electrical wiring. Results showed that the header-riser collector which results in a more homogenous temperature distribution is better than serpentine collector and generates more electrical power. Simulations were performed on seven different collector configurations to determine the best absorber design which gives the highest efficiency [32]. Results show that the spiral flow design gives the highest combined PVT efficiency. However, no analytical model is present in literature for the spiral flow collector design analysis, additionally, there is considerable pressure drop for the spiral flow design. A new collector configuration [33] was suggested along with a collector tube cross-section [31]. This collector configuration is a combination of header-riser and serpentine configurations whereas the proposed tube cross-section will provide a higher a higher contact surface area for heat transfer.

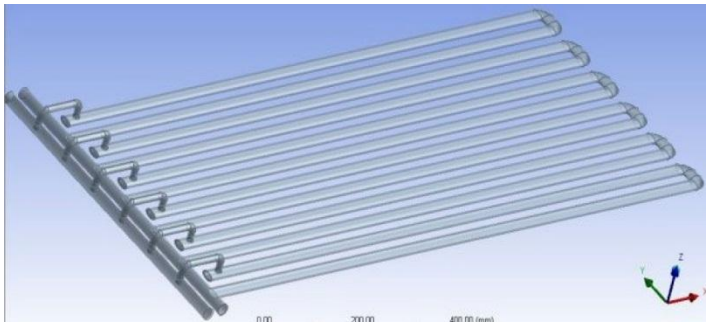

Figure 2.8 New collector configuration for PVT collector

Figure 2.9 Collector tube cross-section

2.4 Use of nanofluid in PVT collector

The fluid which is used to cool the PV cells has a significant impact on the overall performance of PVT system. Earlier designs of PVT system used either air or water as a coolant. Air-based PVT systems were found to have lower thermal efficiencies due to lower heat transfer coefficients and poor heat transfer [34,35]. However low thermal conductivity of fluids used in solar systems such as water or ethylene glycol has been one of the primary limitations to the efficiency improvement of such systems. One of the techniques used to overcome this limitation is the use of nanofluids as the heat transfer fluids in solar collectors. Nanofluids consist of nano-sized particles suspended in base fluids such as water or oil. Owing to their small size the nanoparticles always remain in suspension and even the introduction of a small fraction of nanoparticles greatly enhances the thermal properties of base fluids. Thus the usage of nanoparticles improves the thermophysical properties of base fluids such as thermal conductivity, specific heat capacity and viscosity resulting in an overall enhancement in the fluid's heat transfer coefficient.

In nanofluid-based systems, various factors must be considered such as the type of nanoparticles, type of base fluid, nanoparticle volumetric concentration, nanoparticle size, the stability of nanofluid, the cost of producing nanoparticles and the pumping power required. Nanofluids are not simple mixtures of base fluid and nanoparticles since the nanoparticles tend to aggregate over time and such aggregation may cause blockage of flow channels which will result in a decrease in thermal conductivity of nanofluids [36]. The addition of surfactants have shown to enhance the stability of nanofluids [37];

however, in heat transfer applications surfactants tend to form a foam which degrades the thermal properties of nanofluids [37]. The manufacturing of nanoparticles is complicated; consequently, the cost of production for nanoparticles is high [1]. The increase in the nanoparticle volumetric concentration leads to an increase in the viscosity of nanofluid which leads to an increase in the pressure drop and the required pumping power [38]. Since higher nanoparticle volumetric concentration leads to aggregation of nanoparticles, increased cost and higher pumping power; lowest possible volumetric concentration of nanoparticles should be used along with a surfactant in order to stabilize the nanofluid. On the other hand, it has been shown through various experimental [39,40] and numerical studies [41–43] that increasing the volumetric concentration of nanoparticles enhances the thermal properties and the heat transfer coefficient of nanofluids. Hence, the optimum volumetric concentration of nanoparticles in a nanofluid is different for different nanofluids.

Nanoparticle size is an important factor which contributes to the stability of nanofluids as well as their thermal properties. Experimental [39,40] and analytical studies show that decreasing nanoparticle size increases the thermal conductivity of nanofluids; however, decreasing the nanoparticle size increases cost of production of nanoparticles and instability of nanofluid. The optimum nanoparticle size in a nanofluid is different for different nanofluids. Thermal properties of a nanofluid depend not only on the thermal properties of nanoparticles but also on the properties of the base fluid. Among the most commonly used base fluids, water has the highest thermal conductivity [44]. This, coupled with the fact that water-based nanofluids are generally more stable [45], makes water as

the most suitable choice for base fluid in a nanofluid [40,46].

Selection of the type of nanoparticle in the context of the solar thermal application is critical as it determines not only the thermal properties of nanofluid but also the volumetric concentration and the size of nanoparticles in nanofluid, which in turn determines the pressure drop (pumping power) and the cost of nanofluids. Nanoparticles enhance the thermal conductivity of base fluids which in turn enhance heat transfer. An experimental investigation was carried out for a PVT system which uses water-SiO_2 nanofluid as a coolant at a flow rate of 30 kg/h with the nanofluid having nanoparticles of size 11-13 nm and concentrations of 1 and 3 wt% [47]. Results show an increase of 9.01% and 9.75% in electrical efficiency relative to an uncooled PV system; an increase of 7.6% and 12.8% in thermal efficiency relative to a water-cooled PVT system and an increase of 22.61% and 24.31% in exergy efficiency relative to an uncooled PV system for concentrations of 1 and 3 wt% in a water-SiO_2 based PVT system.

An experimental investigation was performed to compare the thermal conductivities of water-TiO_2 and water-ZnO nanofluids for volume concentrations of up to 3% and the nanoparticle size ranging from 10 to 70 nm with 0.05 M of Sodium Dodecyl Sulfate (SDS) surfactant added to stabilize nanofluid [40]. Results show an enhancement of 20% and 15%, relative to water, in the thermal conductivities of water-ZnO and water-TiO_2 nanofluid, with both nanofluids being stable at 3% volumetric concentration and 30 nm particle size. Experimental and numerical testing was performed on a 40W-PVT system in which nanofluids: water-Al_2O_3, water-ZnO and water-TiO_2 were supplied to the system at

a rate of 30 kg/h. Results show that water-ZnO nanofluid at a concentration of 0.2 wt% and particle size of 10-25 nm, results in maximum improvement in the electrical and thermal performance of PVT system among all the other fluids. An experimental study was performed to compare the effect of five nanofluids: water-CuO, water-Al_2O_3, water-TiO_2 and water-SiO_2 on the performance of a flat plate solar collector (FPSC)[48]; results showed that water-CuO nanofluid at 0.75% volumetric particle concentration and an average particle size of 32 nm gave the maximum improvement in performance. Numerical simulation was performed to investigate the effect of four nanofluids: water-Cu, water-Al_2O_3, water-CuO, and water-Ag on the performance of an FPSC for a nanoparticle volumetric concentration of 1 to 5% [42]. Results show that the use of water-Ag nanofluid at a volumetric concentration of 5% yields the best thermal performance, however, no information was provided about the nanoparticle size or the stability of nanofluid. With the exclusion of the more complicated carbon-based nanoparticles, the addition of silver (Ag) nanoparticles to the base fluid (water) appear to result in a high thermal conductivity of nanofluids [1] and water-Ag nanofluids have been successfully implemented in experimental studies for both FPSCs [2] and PVT systems [3].

The addition of nanofluids affects the density and viscosity of base fluid which in turn affects pressure drop and pumping power. A theoretical analysis was performed on an FPSC using water-Al_2O_3 nanofluid with nanoparticle volumetric fractions of 0.05-0.1% and nanoparticle size of 13 nm [45]. Results show that there is a negligible effect of nanofluid on the pumping power and it is essentially similar to water.

As mentioned earlier surfactants are important to maintain the stability of nanofluids. An experimental investigation was performed to determine the heat transfer enhancement for a water-Ag nanofluid having nanoparticles of size 95 nm and concentration of 0.5wt% stabilized by potassium oleic surfactant (OAK^+) [49]. Results show that a heat transfer enhancement of 80% over water is achieved using 1 wt% of OAK^+ surfactant with better stability and superior thermal properties of nanofluid.

2.5 Real scale application and economic analysis of PVT systems

Both experimental and analytical studies showed that the flat plate PVT solar collector is a promising alternative system for low-temperature applications, which requires electrical energy and heat. Since it was the consumer's demand for energy that triggered research on PVT systems, therefore the success of PVT systems can only be judged in context with real-scale project applications. A significant amount of research [43,50–52] on the actual full-scale implementation of PVT systems, especially with context to buildings, has been performed giving rise to the term Building Integrated PVT (BIPVT) systems. Numerical simulation performed for a PVT system used in 12 sample houses for the climate of Tokyo showed that the reduction in primary fuel consumption resulting from the use of PVT system is 1.5-2 times larger than individual PV or solar water heating system for the same area [51].

According to PVT roadmap [21], the major market potential for PVT system lies in the domestic sector, and therefore to convince domestic or commercial users to invest in PVT systems, one has to accentuate the potential economic benefits from PVT systems.

Therefore, BIPVT studies are usually accompanied with economic analysis. Since additional energy is obtained in a PVT system for the same area as compared to a PV system, the energy cost savings of a PVT system are much higher, hence the payback period of a PVT system is lower than that of a PV system [53]. The thermal and economic analysis was performed for a BIPVT system augmented with an FPSC for a typical domestic application with an electrical energy demand of 3 kW.hr/day and hot water demand of 100 liters/day for the climate of Chennai, India [52]. Results estimated the payback period of the proposed system to be 5 years. A techno-economic analysis was conducted for a water-cooled PVT system which caters to the electricity and hot water needs of a typical house in London, UK [50]. The proposed system which covers 51 % of the household's electrical load and 36 % of the hot water demand, has a life of 20 years, a discounted payback period of 11.2 years and reduces the fossil-fuel consumption by 18%.

Among the available economic models, Life Cycle Cost (LCC) analysis is considerably popular in the analysis of PVT systems [12,54,55]. Since the value of money decreases with time, the time value of money must be considered when determining the feasibility of an investment. The LCC represents the total cradle-to-grave cost of a system expressed in the present value of money. This type of analysis provides effective cost estimation of the system and helps in the determination of the reduction in Cost of Energy (COE) from the use of proposed system.

LCC analysis was performed for a rooftop-fitted, air-cooled BIPVT system to generate electrical energy and hot air for space heating, for the climate conditions of New Delhi,

India [56]. Results predict that the COE from the use of air-cooled BIPVT system is only slightly lower than the cost of unit power from the conventional grid. LCC analysis of a water-cooled BIPVT system installed to support the electricity and hot water demand of an office building, for the climate of Hong Kong, estimates that the proposed system, which has a life of 20 years, will have a payback period of 14.7 years. Numerical simulation of a PVT system for the house was performed for the climate conditions of Nicosia, Cyprus [54]. PV cooling results in the improvement of electrical efficiency from 2.8 % to 7.7 % with the system covering 49 % of the house's hot water needs and has an estimated payback period of 7.6 years.

In this study LCC model was used to demonstrate the economic feasibility of the system through the following indicators: Internal rate of return (*IRR*), Cost of energy (*COE*) and Cost payback time (*CPBT*).

2.6 Use of Thermal storage and Phase Change Material

Solar energy is a time-dependent source of energy and it is available only during daylight hours, however, the thermal load of the building is independent of ambient conditions and may be intermittent depending entirely on building resident's habits. This mismatch in energy supply and demand leads to the ineffective removal of heat from the system. The case is particularly severe when the thermal load of the building is entirely restricted to dark hours. In such cases, the only option left is to incorporate a thermal storage device in this system. Ideally, the storage should remove all the heat gained by the system during daylight hours and, similarly, discharge all the heat as a thermal load. This will make the

performance of the system independent of the temporal variations in thermal load and available thermal energy. This would also lead to the best possible utilization of the benefits gained through the solar system. Since both the electrical and thermal performance of a system depends upon the efficient removal and delivery of thermal energy, thermal storage devices are one of the most critical parts of the PVT system.

The thermal storage device typically consists of a material which stores thermal energy in one of the following three forms: reversible thermochemical energy, sensible thermal energy, and latent thermal energy. Hot water storage tanks which store thermal energy in the form of sensible thermal energy are more popular, both in active and passive PVT systems [12,57,58]. Molten salts have also been used to store thermal energy for high temperature applications[58]. However, among the three forms, a relatively large amount of energy can be stored as latent energy [59]. Materials which store thermal energy in the form of latent heat are known as Phase Change Materials (PCMs). The use of PCMs in thermal storage units have given rise to the term "*thermal battery*". In addition to the considerable amount of thermal energy which can be stored in PCM as latent heat, the isothermal nature of the storage process means that PCM can be used to mediate temperature fluctuations in the thermal energy source to ensure that the optimum operating conditions are met.

Various numerical and experimental studies have been performed to analyze the performance of PCM-Latent heat storage systems. CFD simulation was performed for a shell-and tube thermal storage system in which the PCM sodium nitrate was utilized to

extract energy from and discharge energy to a heat transfer fluid [60]. Numerical analysis for a PCM-thermal storage device was performed in which air was used as working fluid [61]. CFD simulation was performed for a mobile thermal battery in which lithium nitrate was used as PCM and metallic mesh was used to enhance heat transfer within the battery [62]. Thermal analysis and experimental testing was performed for a portable thermal battery (shown in Figure 3.6) which used erythritol as PCM [63]. The current study uses the same design and mathematical model of thermal battery.

During the design of a PCM thermal energy storage, the first decision is the type of phase change to be employed. Solid-liquid, solid-gas, solid-solid or liquid-gas are available as phase transformations. To make the system as simple and as compact as possible (allow minimum variations in volume during phase change), solid-solid or solid-liquid phase transformations should be employed. Generally, solid-liquid phase change yields higher latent heat than solid-solid phase change. The major constraint in the design of a PCM thermal energy storage is the selection of phase change temperature (melting point).

The second law of thermodynamics states that the driving force for heat transfer is a temperature difference. As shown in Figure 1.1 and Figure 1.2 temperature difference is important for both charging (heat addition) and discharging (heat removal) of PCM thermal energy storage. Hence the PCM phase change temperature should be sufficiently below the input temperature of the heated collector fluid to remove as much heat from the fluid as possible. However, the PCM phase change temperature should also be sufficiently higher than the required desired temperature of the domestic water which makes up the thermal

load. In low-temperature, flat-plate systems it is not possible to meet both the requirements, hence a compromise must be made. If the solar system is a hybrid electric/thermal (PVT) device than the effect on the electrical subsystem must also be considered during the selection of phase change temperature.

Depending on the phase change temperature range, a list of PCM candidates can be compiled. Several types of PCMs are known such as paraffin's, fatty-acids, organic and inorganic salt hydrates, organic and inorganic eutectic compounds. During the selection of a PCM, there are many factors which should be considered. Ideally, a PCM used for latent heat storage should have a high latent heat of fusion and high thermal conductivity for high thermal storage and good heat transfer. They should also be stable, both chemically (have a stable composition) and thermally (thermal properties do not undergo change) over the required number of cooling/heating cycles. Additionally, they should be non-toxic, non-inflammable, undergo a small change in volume upon phase change and are available at a reasonable cost.

Naturally occurring paraffin and paraffin waxes have a high latent heat of fusion in the temperature range from 30ºC to 80ºC which makes them useful for solar applications [64]. Commercial paraffins are also cheap, safe, and undergo a small volume change during phase change [63]. Paraffin waxes also undergo negligible changes in their properties during heating/cooling cycles, are non-corrosive and can be used with various materials [65]. However, paraffins have low thermal conductivity [63] and they are flammable [64]. Paraffins have been found to be compatible with graphite and the use of expanded graphite

foams as a form-stable matrix for paraffin based PCMs has shown an increase in the effective thermal conductivity of the PCM [59]. In this study, an organic paraffin wax known as Octadecane, with a phase change temperature of 28 ºC, has been used [65].

2.7 Chapter summary

The key findings of the literature review are:

- Rising energy demands and rapid consumption of fossil fuels has accelerated the development of renewable energy resources in the Kingdom. Because of its location on the Sun-belt, Saudi Arabia is geographically suitable for the solar energy production.
- The electrical output of a PV cell decreases with increasing cell temperature and the use of polycrystalline silicon PV cell is appropriate for current study.
- The use of a solar thermal collector integrated with a PV panel, also known as photovoltaic thermal collector, cools the solar cells providing electricity cat high efficiency and hot fluid simultaneously. Use of a sheet and tube flat-plate collector with active PV cooling (forced convection) is suitable for current study.
- Thermal properties of a fluid can be enhanced by the addition of nano-sized particles. Such fluids are referred to as nanofluids and they have been successfully used in FPSC and PVT systems. Stability and cost must be considered along with property enhancement during the design of nanofluid. Use of silver nanoparticles suspended in water, with a surfactant to stabilize the nanofluid, is suitable for current study.
- Studies involving the practical use of PVT systems are necessary for the successful realization of PVT research. Highlighting potential economic and environmental benefits of PVT systems would further encourage its use.

- The failure of daily residential thermal load profile to correspond with the daily available solar thermal energy profile necessitates the use of a thermal storage. Often the magnitude of the mismatch dictates the use of a latent thermal storage such as PCM-thermal battery. The PCM transition temperature is the most critical factor in the selection of a PCM for thermal storage and it affects both the charging and discharging of thermal battery. Considering both these processes, a PCM having a melting point of 28˚C is considered suitable for this study.

CHAPTER 3

MATERIAL AND CONFIGURATION

3.1 Introduction

To conduct hourly and monthly performance analysis of the system for a residential building in Dhahran, hourly and monthly profiles of input data such as: Meteorological data, residential electricity and hot water consumption are required. Since one of the objectives of the current study is to conduct an economic analysis at the end, each component of the system must be completely defined so that its cost can be estimated. The fluid pump, electric battery and inverter are sized after conducting performance analysis.

3.2 Meteorological data

To determine the thermal and electrical performance of the proposed PVT collector for the whole year for Dhahran, it is necessary to obtain Dhahran's meteorological data for the whole year. The numerical model used in this study requires four types of input data: ambient temperature (T_a), Incident radiation (I) and wind speed (WS) measured at a height of 10 ft. (3.048 m). Experimentally-measured hourly data for the average day of each month (as shown in Appendix A) is used for the year 2014 for Dhahran. This data was provided by the Center for Engineering Research, King Fahd University of Petroleum & Minerals, Saudi Arabia.

3.3 System configuration

The system consists of two subsystems: electrical and thermal. The electrical subsystem consists of a polycrystalline PV module which is connected to an MPPT-equipped charge

controller, a DC-AC solar inverter, and a lead-acid battery. The thermal subsystem consists of a solar thermal collector, fluid pumps, a plate heat exchanger, a PCM containing a thermal battery and an auxiliary heater.

Depending on the time of day the system has two modes of operation: one during sunlight hours and the other during dark hours. At any time, only two of the three fluid pumps are operating together.

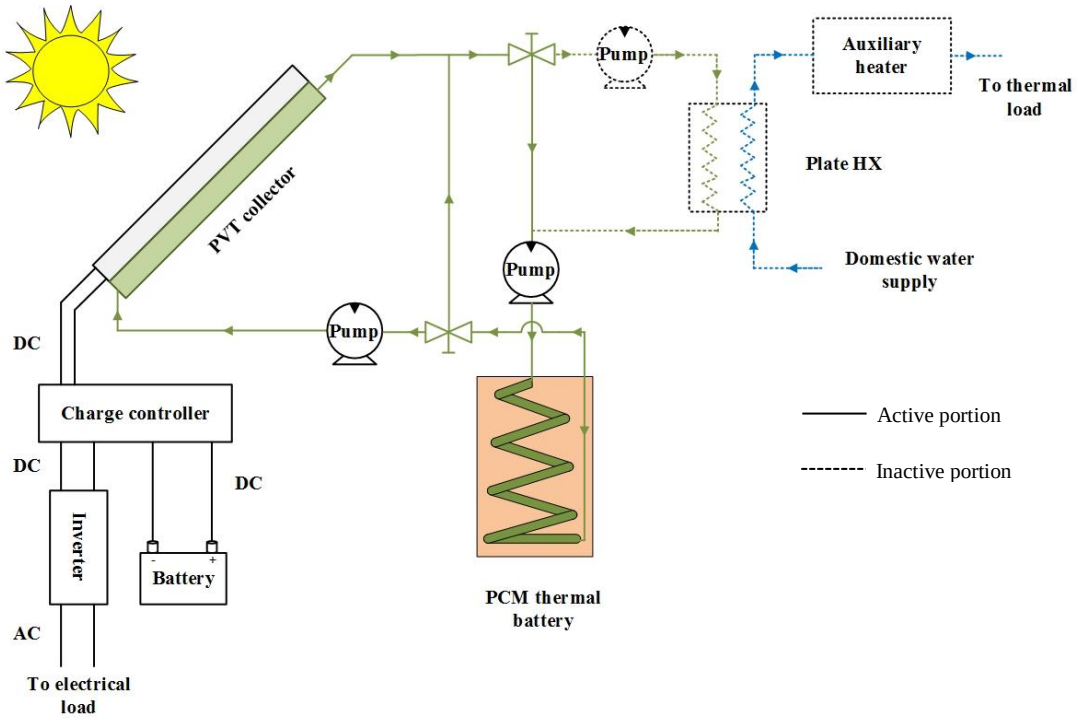

Figure 3.1 Schematic of nanofluid-cooled PVT system with PCM-thermal battery during light hours

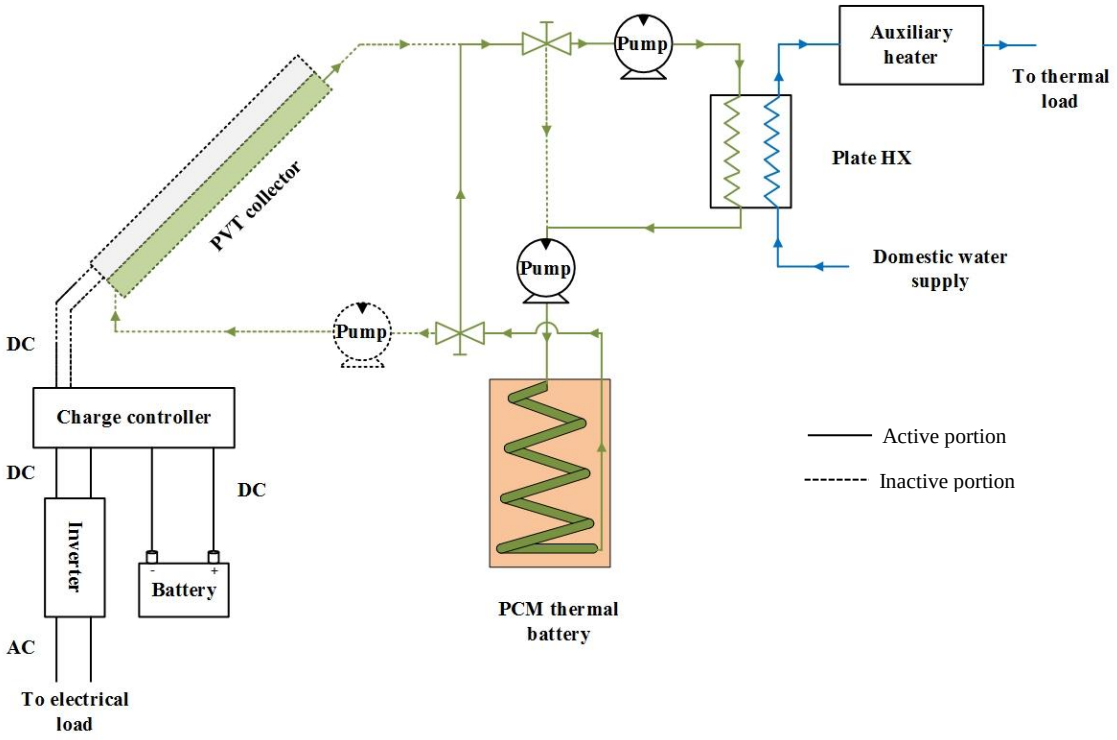

Figure 3.2 Schematic of nanofluid-cooled PVT system with PCM-thermal battery during dark hours

During sunlight hours, a portion of DC electricity produced by PV module, at maximum power conditions, is directed by the controller to the inverter where it is converted to AC. A portion of this AC power is used by the fluid pumps while the rest is consumed by the electrical load. The excess DC electricity produced by PV module is directed by the controller to the electrical battery for storage. The collector fluid, driven by the fluid pumps, absorbs heat from the PV module and loses it to the thermal battery. This heat is stored as latent heat of PCM inside the thermal battery.

During dark hours, electricity stored in the battery is directed by the controller to the inverter where it is converted to AC. A portion of this AC power is used by the fluid pumps while the rest is consumed by the electrical load. The collector fluid, driven by the fluid pump, removes heat from the PCM in thermal battery and loses it to domestic water through

the plate heat exchanger. Domestic water is further heated to the required temperature by the auxiliary heater.

3.4 Load profiles

During the design of the system, it is important to consider the loads applied to the system. It is important to establish that a single PVT unit cannot cover an entire load of a residential building and the purpose of the application of load is to incorporate the temporal variations in load in the design of the system. A PVT system requires both electrical and thermal load, hence both the electricity and thermal load profiles are required. Because of the mismatch in energy supply and demand profiles for both electrical and thermal energies, batteries must be included.

3.4.1 Residential electricity consumption

The simulated hourly electrical load profile for each month was obtained from literature [66] for a residential building in Yanbu shown in the Appendix B. The load was simulated through the popular Renewable energy software HOMER. As stated above, the electrical load of the building is too high to be covered by a single PV module, thus the load is scaled down by a factor of 22 (22 identical solar panels would be required for the building's actual load) so that it is appropriate to the size of this system.

3.4.2 Residential hot water consumption

The forecasted hourly hot water load profile for each month was obtained from literature [67] for a residential building in UK shown in the Appendix C. The profile shows that the hot water demand during the sunlight hours is (7:00 A.M. to 4:00 P.M.) is almost non-existent with demand peaks at 6:00 A.M. (early morning) and 5:00 P.M. (late afternoon).

In the case of such profiles, some form of thermal storage system must be incorporated in the design which would remove heat from the system during sunlight hours and expend it during demand hours. It should be noted that the while the actual electrical load of the building was quite high and needed to be scaled down, the actual thermal load of the building, in terms of mass flow rate, it is not that high. Hence the actual and not the scaled load is applied. However, domestic water can only be heated through the plate heat exchanger to a maximum temperature of 28 ˚C (melting point of PCM used) and it is heated to the required temperature (50 ˚C) through the auxiliary electric water heater.

3.5 PV module and charge controller

Figure 3.3 Enhance XP polycrystalline solar panel

The PV module is made of polycrystalline silicon with a rated power of 275 W and an annual performance degradation rate of 1 %. Its characteristics are listed in Table 3.1.

Table 3.1 Typical electrical characteristic of Enhance XP polycrystalline PV module

Electrical performance under Standard Test Conditions (S.T.C)

Model		Enhance XP-275
Cell Type		Polycrystalline
Dimension		1640mm x 992mm
Rated power	P_{max}	275 W
Open-circuit voltage	$V_{oc,ref}$	38.63 V
Short-circuit current	$I_{sc,ref}$	9.23 A
Voltage at P_{max}	$V_{mp,ref}$	31.1 V
Current at P_{max}	$I_{mp,ref}$	8.85 A
PV module electrical efficiency	$\eta_{mp,ref}$	16.9 %
Number of cells	N_s	60
Open-circuit voltage temperature coefficient	μ_{Voc}	-0.1209 V/K
Short-circuit current temperature coefficient	μ_{Isc}	0.004246 A/K
STC: Irradiance 1000 W/m^2, AM 1.5 spectrum, module temperature 25˚C		

The charge controller is equipped with a Maximum Power Point Tracker (MPPT).

3.6 Nanofluid

The nanofluid consists of deionized water containing 0.5 vol% of silver nanoparticles and 1 wt% of potassium oleate surfactant (OAK+). It was prepared by sonicating in a water

bath with a cooling technique for a period of 12 hours to reduce the average nanoparticle size to 10 nm [49].

Table 3.2 Nanofluid specifications

Nanoparticle		Silver (Ag)
Nanoparticle size	d_p	10 nm
Nanoparticle concentration	Φ_{nf}	0.5 vol%
Boiling temperature of base fluid	T_b	100 ˚C
Base fluid		Deionized water
Surfactant		Potassium oleate (OAK^+)
Surfactant concentration		1 wt%

3.7 Collector

The collector consists of a 1 mm stainless steel absorber plate attached to a hybrid parallel-serpentine collector also made of stainless steel. Five hairpin tubes are welded on to the absorber with each tube having a modified cross section (see Figure 6.10) with a width of 76 mm, a height of 11.4 mm and a thickness of 1 mm. The absorber is attached to the PV panel by means of a paste which has very high thermal conductivity and very low electrical conductivity. The entire PVT collector is encased in an aluminum frame with polyurethane foam as insulation.

Figure 3.4 Collector configuration

Table 3.3 Specifications of PVT collector with assumed working conditions

Tube spacing	W_{coll}	91 mm	Absorber conductivity	k_{abs}	51 W/m.K
Collector area	A_c	1.627 m^2	Absorber thickness	δ_{abs}	1 mm
Number of serpentine channels	N_{ch}	5	Inner hydraulic diameter of tube	d_i	16.6 mm
Emittance of glass	ε_g	0.88	Outer diameter of tube	d_o	18.6 mm
Emittance of plate	ε_{abs}	0.95	Insulation conductivity	k_b / k_e	0.045 W/m.K
Emittance of PV	ε_{PV}	0.95	Glass thickness	δ_g	3.2 mm
Tilt (slope)	β	26º	Glass extinction coefficient	K_g	16.1 m^{-1}
EVA thickness	δ_{EVA}	0.5 mm	Glass refractive index	n_g	1.526
EVA conductivity	k_{EVA}	0.35 W/m.K	Fluid flow rate	m_{fluid}	0.0784 kg/s
Glass conductivity	k_g	1.8 W/m.K	Length of hairpin		1.5 m

Absorber transmittance-absorptance product	$(\tau\alpha)_p$	0.84	Absorber conductivity	k_{abs}	51 W/m.K
PV absorptance	α	0.9	Absorber thickness	δ_{abs}	1 mm

3.8 Heat exchanger

Figure 3.5 Lytron LL510G12 Liquid-to-Liquid copper brazed plate heat exchanger

The heat exchanger is a copper liquid-to-liquid brazed plate heat exchanger which removes heat from the collector fluid and passes it to domestic water.

Table 3.4 Heat exchanger specifications

Type		brazed plate liquid-to-liquid
Model		Lytron LL510G12
Mass flow rate of cold water	m_w	0.0523 kg/s
Plate enlargement factor	Φ_{hxg}	1.25
Number of plates	$N_{p,hxg}$	10

Length	L_{hxg}	170 mm
Width	W_{hxg}	74 mm
Port diameter	D_{hxg}	20 mm
Plate thickness	$\delta_{p,hxg}$	0.6 mm
Plate conductivity	k_{hxg}	13.32 W/m.K
Plate chevron angle		45˚

3.9 Thermal Battery and PCM

The thermal battery used in this design was fabricated and experimentally tested and all the dimensions are obtained from the literature [63]. The battery consists of three components: PCM material (10 kg of Octadecane), a stainless-steel storage tank (280 mm in both height and diameter) and a copper helical coiled tube (AS1432—12.7 mm diameter with a 1 mm thickness, a 7m length). The entire battery is packed with thermal insulation (Superwool 607 Blanket) with a total energy capacity of 0.7 kWh and a total cost of 528 AUD (US$ 398).

Table 3.5 Thermal battery specifications

Tube inner diameter	$d_{i,TB}$	0.0107 m
Tube outer diameter	$d_{o,TB}$	0.0127 m
Coil height	H_{TB}	0.22 m
Coil radius	R_{TB}	0.1 m
Coil surface area	$A_{s,TB}$	0.2793 m^2

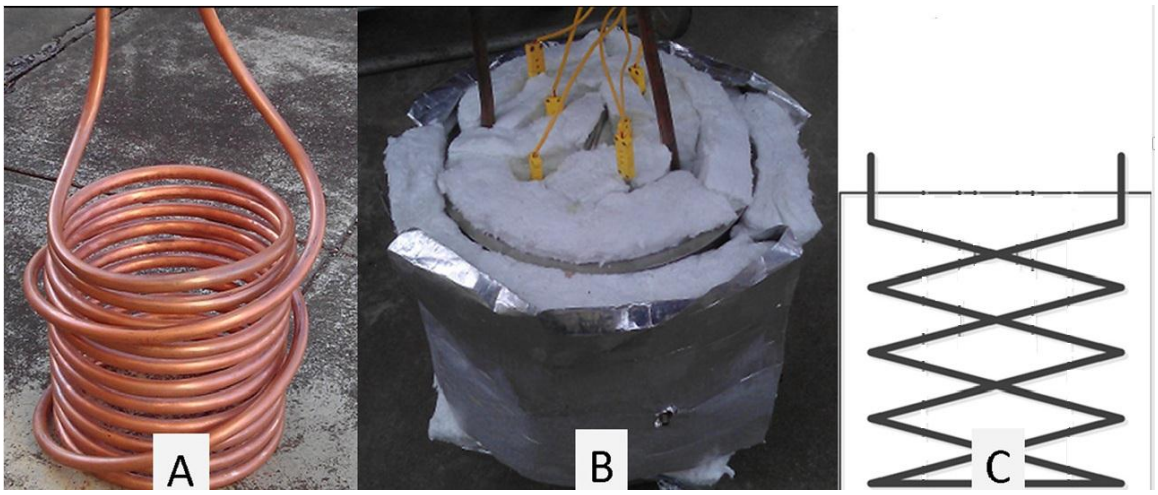

Figure 3.6 Battery design—(a) coiled copper tubing, (b) final insulated thermal battery design, and (c) battery schematic

Octadecane is an organic paraffin wax and its properties have been obtained from literature [65]. Octadecane, like most paraffin materials, is a naturally occurring which is non-corrosive, non-toxic with high latent heat of fusion and is chemically and thermally stable (negligible changes in properties during heating/cooling cycles). Like other paraffin waxes, it has low thermal conductivity, however, the use of expanded graphite foams as a form-stable matrix for paraffin based phase change materials has resulted in an increase in the effective thermal conductivity of the phase change material [59].

Table 3.6 Phase change material specifications

PCM	Octadecane	
Melting point	T_{PCM}	28 ˚C
Latent heat of fusion	$h_{sl,PCM}$	244 kJ/kg
Thermal conductivity	k_{PCM}	0.21 W/m.K
Density	ρ_{PCM}	774 kg/ m^3
Specific heat capacity	$c_{p,PCM}$	1.9 kJ/kg.K
Mass	m_{PCM}	10 kg

CHAPTER 4

METHODOLOGY

4.1 Assumptions

- Altitude of system is 10 m above ground
- Perfect thermal contact is assumed between PV and collector
- Charge controller is assumed to be equipped with MPPT
- Hellman coefficient is assumed to be 0.40 for stable air above flat open coast
- The fraction of radiation reflected from ground is assumed to be 0.2
- Parts of collector and heat exchanger are assumed to be thin enough to have negligible masses and heat capacitances to ignore the transient effects.
- The PV module is assumed to be fixed, i.e. no solar tracking, tilted at an angle equal to the Dhahran latitude (β=26˚) and facing south, i.e. azimuth angle is 0˚.
- The collector fluid (nanofluid) is assumed to have a constant mass flow rate of 0.078 kg/s for every hour.
- The thermal battery is assumed to be completely thermally insulated.
- The thermal battery has been analyzed solely as a heat exchanger and the analysis of melting or solidification of PCM has not been considered [63].
- The thermal battery is completely insulated and the whole PCM is initially at its melting temperature [63].
- Battery efficiency, inverter efficiency power factor are assumed to be 0.85, 0.9 [68] and 0.8 respectively.
- Thermal residential load in Saudi Arabia is covered with an electric water heater.

- 100% of the total investment cost is paid at the beginning.
- Annual maintenance cost, *MC*, is assumed to be the sum of 2.76 % of PV cost, 2.3 % of heat exchanger cost and 0.7 % of pump cost [57].
- Battery and inverter are to be replaced after 7 years [55].

4.2 Absorbed radiation and optical model

Incident radiation values for each hour of the representative date of each month for Dhahran, Saudi Arabia can be determined from appendix A. Since incident radiation (*I*) values were measured using a horizontally-set pyranometer and the PVT collector is tilted at an angle, it is necessary to calculate total radiation (I_T) and absorbed radiation (S) from incident radiation (*I*).

Based on the Isotropic diffuse sky model derived by Liu and Jordan (1963) [69] total radiation incident on a tilted surface (I_T) is calculated by

$$I_T = I_b R_b + I_d \left(\frac{1 + cos\beta}{2}\right) + I\rho_g \left(\frac{1 - cos\beta}{2}\right) \quad (4.1)$$

where ρ_g is the ground reflectance and is assumed to have a value of 0.2. I_b and I_d are direct and diffuse radiation and β is the collector tilt angle.

R_b is the ratio of direct radiation on tilted surface to that on a horizontal surface and can be calculated by:

$$R_b = \frac{cos\theta_1}{cos\ \phi\ cos\delta\ cos\omega + sin\ \phi\ sin\ \delta} \quad (4.2)$$

where ϕ is latitude of Dhahran, δ is the declination angle, ω is the average hour angle between two hours and θ_1 is the incidence angle.

$$\theta_1 = cos^{-1}(cos\delta\ cos\omega) \tag{4.3}$$

For the determination of I_b and I_d, we first need to determine the extra-terrestrial hourly radiation on a horizontal surface (I_{ET})

$$I_{ET} = \frac{12 \times 3600}{\pi} G_{sc} \left(1 + 0.033\ cos\frac{360n}{365}\right) \times \left[cos\delta\ cos\phi\ (sin\omega_2 - sin\omega_1) + \frac{\pi(\omega_2 - \omega_1)}{180} sin\ \phi\ sin\ \delta\right] \tag{4.4}$$

where G_{sc} is the solar constant with a value of 1367 W/m^2 ω_2 and ω_1 are the hour angles between which is the period of interest (e.g to find the hourly radiation for 11 AM the hour angles would be those corresponding to 11 AM and 12 noon), n is the number of days and ω is the average of ω_2 and ω_1.

The declination angle, δ and number of the day, n for the representative date of each month are shown in Appendix B. The meteorological data in Appendix A is also calculated for these dates only.

Next the hourly clearness index, k_t, which is the ratio of incident radiation (I) and extra-terrestrial hourly radiation (I_{ET}), is determined

$$k_t = \frac{I}{I_{ET}} \tag{4.5}$$

Next, the ratio of diffuse hourly radiation (I_d) to incident hourly radiation (I) is determined using the Erbs et al (1982) correlation [69] to determine the diffuse hourly radiation (I_d)

$$\frac{I_d}{I} = 1 - 0.09k_t \quad \text{for } k_t \leq 0.22 \tag{4.6}$$

$$\frac{I_d}{I} = 0.9511 - 0.1604k_t + 4.388{k_t}^2 - 16.638{k_t}^3 + 12.366{k_t}^4 \quad \text{for } 0.22 \leq k_t \leq 0.80 \tag{4.7}$$

$$\frac{I_d}{I} = 0.165 \quad \text{for } k_t > 0.8 \tag{4.8}$$

Incident radiation (I) is the sum of direct and diffuse portion of radiation, so I_b can be determined by

$$I_b = I - I_d \tag{4.9}$$

Based on the Isotropic diffuse sky model derived by Liu and Jordan (1963) [69], solar energy absorbed by a tilted collector absorbed plate, S can be found by:

$$I_T = I_b R_b (\tau\alpha)_b + I_d (\tau\alpha)_d \left(\frac{1 + cos\beta}{2}\right) + I\rho_g (\tau\alpha)_g \left(\frac{1 - cos\beta}{2}\right) \tag{4.10}$$

where, $(\tau\alpha)_b$, $(\tau\alpha)_d$, $(\tau\alpha)_g$ are the beam, diffuse and ground-reflected transmittance-absorptance products. Their values depend on the optical properties of glazing material (glass) and the incident angle of the incident radiation.

The transmittance-absorptance products are determined using the following approximation:

$$(\tau\alpha) \cong 1.01\tau\alpha \tag{4.11}$$

where τ is the transmittance of glass and α is the absorptance of PV cell. The PV absorptance remains constant, however, the glass transmittance depends on the angle of radiation. The glass transmittance $(\tau\alpha)_b$ is determined from θ_1, $(\tau\alpha)_d$ is determined from θ_d and $(\tau\alpha)_g$ is determined from θ_g, where Θ_d and Θ_g can be calculated using the Brandemuehl and Beckman (1980) relation [69] for calculating effective incidence angle based on the Isotropic diffuse sky model

$$\theta_g = 90 - 0.5788\beta + 0.002693\beta^2 \quad (4.12)$$

$$\theta_d = 59.7 - 0.1388\beta + 0.001497\beta^2 \quad (4.13)$$

The relationship between glass transmitted τ and angle of radiation θ is described as follows:

$$\tau = \tau_a \tau_r \quad (4.14)$$

$$\tau_a = \tau_a e^{-K_g L_g} \quad (4.15)$$

where K_g is the extinction coefficient of glass and L_g is the thickness of the glass

$$\tau_r = \frac{1}{2}\left(\frac{1 - r_{||}}{1 + r_{||}} + \frac{1 - r_{\llcorner}}{1 + r_{\llcorner}}\right) \quad (4.16)$$

$$r_{||} = \frac{\left(tan(\theta_2 - \theta)\right)^2}{\left(tan(\theta_2 + \theta)\right)^2} \quad (4.17)$$

$$r_{\llcorner} = \frac{\left(sin(\theta_2 - \theta)\right)^2}{\left(sin(\theta_2 + \theta)\right)^2} \quad (4.18)$$

where n_g is the refractive index of glass and θ is θ_1 or θ_d or θ_g depending on which transmittance absorptance product is being calculated.

4.3 Electrical model for PV system

The electrical and thermal analysis depend on each other since a portion of the incident energy is converted into electrical power and the remaining is converted to thermal power. To find output values such as maximum power point voltage (V_{mp}), maximum power point current (I_{mp}), maximum power (P_{mp}) and maximum power point efficiency (η_{mp}) an electrical model is used. These values are determined using the five-parameter model [17] in Appendix D.

The five unknown parameters are of the model are ideality factor (a), light generated current (I_L), diode reverse saturation current (I_o), series resistance (R_s) and shunt resistance (R_{sh}).

The electrical power P_{mp}, and efficiency, η_{mp} will be:

$$P_{mp} = I_{mp}V_{mp} \tag{4.19}$$

$$\eta_{mp} = \frac{P_{mp}}{I_T A_c} \tag{4.20}$$

where A_c is the collector area and can be determined by the product of the length, L_{PV}, and width, W_{PV} of the PV panel.

4.4 Silver/water nanofluid's properties model

The four nanofluid properties necessary for the calculation of heat transfer and pressure drop across the PVT collector and heat exchanger are nanofluid density ρ_{fluid}, nanofluid viscosity μ_{fluid}, nanofluid specific heat capacity $c_{p,fluid}$ and nanofluid thermal conductivity k_{fluid}. The correlation for the determination of ρ_{fluid} [70], μ_{fluid} [71] and $c_{p,fluid}$ [72] are relatively straightforward

$$\rho_{fluid} = \varphi_{nf}\rho_n + \left(1 - \varphi_{nf}\right)\rho_f \tag{4.21}$$

$$\mu_{fluid} = \left(1 + 2.5\varphi_{nf}\right)\mu_f \tag{4.22}$$

$$c_{p,fluid} = \frac{c_{pn}\varphi_{nf}\rho_n + \left(1 - \varphi_{nf}\right)\rho_f c_{pf}}{\varphi_{nf}\rho_n + \left(1 - \varphi_{nf}\right)\rho_f} \tag{4.23}$$

The calculation of k_{fluid} however, requires the use of a correlation known as the Vaschy-Buckingham theorem [39] (Appendix E) which has shown to be in excellent agreement

with the experimentally measured thermal conductivity values for a wide range of nanofluids.

4.5 Thermal model for PVT collector

The mathematical model described below is a one-dimensional steady-state model. The thermal performance of a PVT collector is determined in terms of parameters such as useful thermal energy Q_u, thermal efficiency (η_{th}) and fluid outlet temperature (T_o). Useful thermal power (Q_u) is determined using the following Hotel-Whillier equation [69]:

$$Q_u = F_R A_c \left[(\tau\alpha)_p \left(S - I_T \eta_{mp}\right) - U_L \left(T_i - T_a\right)\right] \quad (4.24)$$

where $(\tau\alpha)_p$ is the transmittance-absorptance product of absorber plate, F_R is the collector heat removal factor, U_L is the overall heat loss coefficient, T_i is the fluid inlet temperature and T_a is the ambient temperature.

$$\eta_{th} = \frac{Q_u}{I_T A_c} \quad (4.15)$$

$$T_o = T_i + \frac{Q_u}{c_{p,fluid}\, \dot{m}_{fluid}} \quad (4.26)$$

where T_o is the fluid outlet temperature, $\dot{m}_{fluid}$ is the mass flow rate of fluid to the collector and $c_{p,\,fluid}$ is the specific heat capacity of collector fluid.

To determine F_R for the Hotel-Whillier equation, first, it is necessary to determine the overall loss coefficient, U_L, which is a sum of top loss coefficient, U_t, bottom loss coefficient, U_b and edge loss coefficient, U_e

$$U_L = U_t + U_b + U_e \quad (4.27)$$

Back loss coefficient, U_b can be calculated from

$$U_b = \frac{k_b}{\delta_b} \tag{4.28}$$

where δ_b is the back insulation thickness and k_b is the back insulation thermal conductivity.

Edge loss coefficient, U_e can be calculated from

$$U_e = \frac{k_e}{\delta_e} \tag{4.29}$$

where δ_e is the edge insulation thickness and k_e is the edge insulation thermal conductivity.

Top loss coefficient, U_t can be calculated from

$$U_t = \left[\frac{\delta_g}{k_g} + \frac{\delta_{EVA}}{k_{EVA}} + \frac{1}{h_{r,PV,g}} + \frac{1}{h_{r,p,PV}} + \frac{1}{h_w + h_{r,g,a}}\right]^{-1} \tag{4.30}$$

where L_g is the glass cover thickness, k_g is the glass thermal conductivity, L_{EVA} is the EVA encapsulation thickness and k_{EVA} is the EVA encapsulation thermal conductivity, h_w is the wind convection heat transfer coefficient from glass cover to ambient, $h_{r,PV,g}$ is the radiation heat transfer coefficient from PV cell to glass cover, $h_{r,p,PV}$ is the radiation heat transfer coefficient from absorber plate to PV panel and $h_{r,g,a}$ is the radiation heat transfer coefficient from glass cover to ambient.

Convection heat transfer coefficient from glass cover to ambient h_w depends on the ambient wind speed, WS. h_w can be determined through a Nusselt number correlation for wind heat transfer, Nu_w which can be determined from the following relation found in the literature

$$Nu_w = 0.86\, Re_w^{\,1/2}\; Pr_w^{\,1/3} \tag{4.31}$$

Re_w and Pr_w can be determined using the properties of air at temperature T_w (average temperature of glass temperature, T_g and air temperature, T_a) and WSA (actual wind speed at height of 10 m). Since the wind data available, WS, was measured at a height of 3.048 m, WSA can be determined from the following relation

$$\frac{WSA}{WS} = \left(\frac{z_a}{z}\right)^{\alpha} \tag{4.32}$$

where actual height, z_a is 10 m, reference height, z is 3.048 m and α is the hellman coefficient which is assumed to have a value of 0.4 for stable air above the flat coast.

Radiation heat transfer coefficients from, $h_{r,abs,PV}$, $h_{r,PV,g}$ *and* $h_{r,g,a}$ depends on plate temperature T_{abs}, cell temperature T_{cell} , glass temperature T_g and ambient temperature T_a

$$h_{r,abs,PV} = \frac{\sigma[(T_{abs} + 273)^2 + (T_{cell} + 273)^2][(T_{abs} + 273) + (T_{cell} + 273)]}{\frac{1}{\epsilon_{abs}} + \frac{1}{\epsilon_{PV}} - 1} \tag{4.33}$$

$$h_{r,PV,g} = \frac{\sigma\left[(T_{cell} + 273)^2 + \left(T_g + 273\right)^2\right]\left[(T_{cell} + 273) + \left(T_g + 273\right)\right]}{\frac{1}{\epsilon_{PV}} + \frac{1}{\epsilon_g} - 1} \tag{4.34}$$

$$h_{r,g,a} = \sigma\epsilon_g\left[\left(T_g + 273\right)^2 + (T_a + 273)^2\right]\left[\left(T_g + 273\right) + (T_a + 273)\right] \tag{4.35}$$

where σ is the Stefan-Boltzmann constant and is equal to 5.6697×10^{-8} W/m^2 K^4 and ε_{abs} is the stainless-steel plate emittance, ε_{PV} is the PV cell emittance and ε_g is the glass emittance.

Collector heat removal factor, F_R can be calculated from the Zhang and Lavan model [25] in Appendix F.

Convection heat transfer coefficient is determined from the following Nusselt number correlation for laminar flow in pipes

$$Nu_{fluid} = \frac{d_i\, h_{fluid}}{k_{fluid}} = \left(1.86 Re_{fluid}\, Pr_{fluid}\, \frac{d_i}{L_{fluid}}\right)^{1/3} \tag{4.36}$$

where L_{fluid} is, the length traveled by the fluid in the collector.

Cell temperature T_{cell} can be determined through

$$T_o = T_i + \frac{Q_u}{F_R\, U_L\, A_c}(1 - F_R) \tag{4.37}$$

Absorber plate temperature T_{abs} can be determined through cell temperature T_{cell}

$$T_{abs} = T_{cell} - \left[U_t\,(T_{cell} - T_a)\left(\frac{L_{EVA}}{k_{EVA}} + \frac{1}{h_{r,PV,g}}\right)\right] \tag{4.38}$$

Glass temperature T_g can be determined through cell temperature T_{cell}

$$T_g = T_{cell} - \left[U_t\,(T_{abs} - T_a)\left(\frac{\delta_g}{k_g} + \frac{\delta_{EVA}}{k_{EVA}} + \frac{1}{h_{r,PV,g}}\right)\right] \tag{4.39}$$

Fluid temperature T_{fluid} is the average of fluid inlet temperature T_i and fluid outlet temperature T_o

$$T_{fluid} = \frac{T_i + T_o}{2} \tag{4.40}$$

Nanofluid properties are calculated at fluid temperature.

4.6 Thermal model for PV system (without cooling)

It is important to determine the performance of an uncooled PV module, to compare its performance with that of water-cooled PVT system. In this case, only the equations for the electrical model remain the same, with new equations added as part of the thermal model

$$T_{cell} = T_{cell} - \left[SU_t\left(1 - \eta_{mp}\right)\right] + T_a \tag{4.41}$$

$$T_g = T_{cell} - \left[U_t\left(T_{cell} - T_a\right)\left(\frac{\delta_g}{k_g} + \frac{\delta_{EVA}}{k_{EVA}}\right)\right] \tag{4.42}$$

$$U_t = \left[\frac{\delta_g}{k_g} + \frac{\delta_{EVA}}{k_{EVA}} + \frac{1}{h_w + h_{r,g,a}}\right]^{-1} \tag{4.43}$$

4.7 Thermal model for thermal battery and heat exchanger

The analytical model for the thermal analysis of thermal battery, from reference [63] is based on the thermal and flow characteristic of the collector fluid flowing in the coiled tube to determine the heat transfer from the fluid to the PCM. The thermal battery has been analyzed solely as a heat exchanger and the analysis of melting or solidification of PCM has not been performed.

The PCM is assumed to be initially at its phase change temperature, hence the thermal boundary condition at the outer surface of the coil is the melting point of PCM, T_{PCM}. Since the tube inside the battery has a helical design, the average Nusselt number of heat transfer in the coiled tube for fully developed flow with constant wall temperature is:

$$Nu_{TB} = \frac{h_{TB}\, d_{i,TB}}{k_{TB}}$$

$$= \left[\left\{ 3.657 + \frac{4.343}{1 + \left[\frac{957}{Pr_{TB}\, He_{TB}{}^{2}} \right]^{2}} \right\} + 1.158 \left\{ \frac{He_{TB}}{1 + \left[\frac{0.477}{Pr_{TB}} \right]} \right\} \right] \quad (4.44)$$

where He_{TB} represents the helical number, which is defined as:

$$He_{TB} = Re_{TB} \sqrt{\frac{d_{o,TB}}{2R_{TB}\left[1 + \frac{H_{TB}}{(2\pi R_{TB})^{2}}\right]}} \quad (4.45)$$

where $d_{i,TB}$, $d_{o,TB}$, H_{TB} and R_{TB} are the helical tube inner diameter, helical tube outer diameter, helical coil height and helical coil radius. Re_{TB}, Pr_{TB} and k_{TB} are Reynold's number, the Prandtl number and the thermal conductivity of the fluid inside the coil and are determined by calculating collector fluid properties at a temperature of $T_{fluid,TB}$

$$T_{fluid,TB} = \frac{T_o + T_{i,t+1}}{2} \quad (4.46)$$

Collector fluid is cooled by the thermal battery to temperature $T_{i,t+1}$. Collector fluid will enter the collector at this temperature for the subsequent hour. From a heat transfer point of view, this design is essentially an insulated heat exchanger. Hence $T_{i,t+1}$ is calculated through the logarithmic mean temperature difference approach:

$$T_{i,t+1} = T_{PCM} + (T_o - T_{PCM})\, e^{-\frac{h_{TB}\, A_{s,TB}}{c_{p,fluid,TB}\, \dot{m}_{fluid}}} \quad (4.47)$$

where $A_{s,TB}$ is the heat transfer surface area of the coil and $c_{p,fluid,TB}$ is the specific heat capacity of collector fluid at a temperature of $T_{fluid,TB}$.

For plate heat exchanger, thermal model from reference [73] has been employed.

4.8 Pressure drop model for system

To determine the size of the pump and the electrical power required to operate that pump to move the collector fluid, pressure drop in the collector heat exchanger and thermal battery must be determined.

Total pressure drop experienced by the fluid is the sum of pressure drop in collector and pressure drop in heat exchanger/ thermal battery

$$\Delta p_{total} = \Delta p_{hxg/TB} + \Delta p_{coll} \tag{4.48}$$

Pressure drop in the collector can be determined using the following correlation [45]:

$$\Delta p_{coll} = \frac{\rho_{fluid}}{2}\left(\frac{4\dot{m}_{fluid}}{\rho_{fluid}\, {d_i}^2}\right)^2 \left[\left(f_{coll}\frac{L_{coll}}{d_i}\right) + (2K_L)\right] + \rho_{fluid}\, L_{PV}\, g \sin\beta \tag{4.49}$$

where L_{coll} is, the distance travelled by the fluid in the collector which is equal to the total length of one serpentine tube, f_{coll} is the friction factor of fluid in the collector, g is the gravitational constant and K_L is the minor loss coefficient due to the U-bend in serpentine tube and has a value of 0.18. Friction factor, f_{coll} can be determined by the following relation for laminar flow:

$$f_{coll} = \frac{16}{Re_{fluid}} \tag{4.50}$$

Pressure drop in the thermal battery can be determined using the following correlation:

$$\Delta p_{TB} = f_{TB} \frac{L_{TB}}{d_{i,TB}} \frac{{V_{fluid,TB}}^2}{2\rho_{fluid,TB}} \tag{4.51}$$

where f_{TB} is the friction factor of collector fluid in the thermal battery and $V_{fluid,TB}$ is the velocity of collector fluid in the thermal battery. f_{TB} and $V_{fluid,TB}$ are determined through the following relations:

$$V_{fluid,TB} = \frac{4\dot{m}_{fluid}}{\pi \mu_{fluid,TB} {d_{i,TB}}^{0.2}} \tag{4.52}$$

$$f_{TB} = \frac{0.336}{{Re_{TB}}^{0.2}} \left[\frac{d_{i,TB}}{2R_{TB}}\right]^{0.1} \tag{4.53}$$

where $\rho_{fluid,TB}$, $\mu_{fluid,TB}$ and $Re_{fluid,TB}$ are the collector fluid density, absolute viscosity and Reynold number at temperature $T_{fluid,TB}$.

Pressure drop in the plate heat exchanger can be determined through reference [73]

4.9 Exergy model

Exergy analysis of a thermal system is important as it helps in identifying the location and magnitudes of thermodynamic inefficiencies within the system. The exergy model used in this study has been obtained from literature [48]. The exergy efficiency can be calculated by:

$$\dot{\eta}_{ex} = 1 - \frac{\dot{E}x_{dest}}{\dot{E}x_{in}} \tag{4.54}$$

where Ex_{in} is the rate of input radiation exergy from the sun and can be calculated by:

$$\dot{E}x_{in} = I_T A_c \left[1 - \frac{4}{3}\frac{(T_a + 273)}{(T_s + 273)} + \frac{1}{3}\left(\frac{T_a + 273}{T_s + 273}\right)^4\right] \tag{4.55}$$

and Ex_{dest} is the rate of exergy destruction and can be calculated by:

$$\dot{E}x_{dest} = \dot{E}x_{in} - \dot{E}x_{th} - P_{mp} \tag{4.56}$$

where Ex_{th} is the rate of output thermal exergy and can be calculated by:

$$\dot{E}x_{th} = (T_a + 273)\left[c_{p,fluid}\,\dot{m}_{fluid}\,\ln\left(\frac{T_o + 273}{T_i + 273}\right) + \frac{\dot{m}_{fluid}}{\rho_{fluid}\Delta p_{coll}}\right] \tag{4.57}$$

4.10 Economic model

The purpose of the economic analysis is to demonstrate the economic feasibility of the proposed system through some key indicators. The three key indicators used in this analysis are **Cost Pay Back** Time (*CPBT*), **Internal Rate of Return** (*IRR*) and **Cost of Energy** (*COE*) generated by the system. *CPBT* is the time it takes for the system to generate enough revenue to recover the total investment cost. IRR is the discount rate, i_d above which the investment will no longer remain feasible. *COE* is the cost per unit electricity generated by the system and it should be lower than the domestic electricity price of the region of interest (COE_i).

The simple cost payback time can be determined by the following relation [55]:

$$CPBT = \frac{IC}{COE_i \times EC_{sav\ per\ year}} \tag{4.58}$$

where *IC* is the total investment cost, COE_i is the domestic cost of electricity and $EC_{sav\ per\ year}$ is the electrical energy saved by the PVT system per year

The economic model used to assess the system in this study is the life cycle cost (LCC) model. Use of LCC model is quite popular in the assessment of PVT systems [12,55,57].

LCC analysis provides the total overall cost of the system, consisting of both present and future costs, expressed in today's money during a given life period

$$LCC_n = \sum_{1}^{n} DCF_Y - IC \tag{4.59}$$

where DCF_Y is the discounted cash flow for year Y and n is the lifetime of the system. DCF_Y is the present value of future cash flow for year Y:

$$DCF_Y = \frac{CF_Y}{(i_d + 1)^Y} \tag{4.60}$$

where i_d is the discount rate and CF_Y is the future cash flow for year Y:

$$CF_Y = EC_{sav,Y} - MC_Y - RC_Y \tag{4.61}$$

where MC_Y is the future value of annual maintenance cost, RC_Y is the future value of annual replacement cost of expired components and $EC_{sav,Y}$ is the future value of the cost of electricity saved by the system. MC_Y and RC_Y of annual are determined by the following relations:

$$MC_Y = MC(1 + i_e)^Y \tag{4.62}$$

$$RC_Y = RC(1 + i_e)^Y \tag{4.63}$$

where MC and RC are the present values of total annual maintenance and replacement cost respectively and i_e is the annual inflation rate of the region of interest. $EC_{sav,Y}$ is calculated as:

$$EC_{sav,Y} = [E_L(1 - D_L)^Y + E_H(1 - D_H)^Y] \times COE_i(1 + i_{ec})^Y \tag{4.64}$$

where E_L and E_H are, the total annual electricity saved for electrical and thermal load respectively, D_L and D_H are the annual performance degradation rate for the PV electrical

and thermal system respectively and i_{ec} is the annual inflation rate of domestic electricity cost of the region of interest.

Uniform annualized life-cycle cost of the system in terms of present value, *ALCC* is the product of life cycle cost, *LCC* and the capital recovery factor, *CRF*:

$$ALCC = CRF \times LCC \tag{4.65}$$

$$CRF = \frac{i_d(i_d + 1)^{np}}{(i_d + 1)^{np} - 1} \tag{4.66}$$

The cost per unit electricity generated by the PVT system, *COE* is the ratio of *ALCC* and the electrical energy saved by the PVT system per year:

$$COE = \frac{ALCC}{EC_{sav\ per\ year}} \tag{4.67}$$

The internal rate of return (*IRR*) can be determined by performing a sensitivity analysis of discount rate, i_d on Life cycle cost (LCC). The value of i_d for which *LCC* is zero is known as the *IRR* and if the current i_d is lower than *IRR* than the system is considered economically feasible.

CHAPTER 5

VALIDATION

Since most of the results in this study were obtained through *analytical* solutions, it is important to validate the analytical models used in this study, *experimentally* or *numerically*. Furthermore, the analytical models used for PVT collector are for **one-dimensional** and **quasi-steady** analysis, so it is important to establish the validity of performing such an analysis in context with the proposed system. The validity of performing a one-dimensional analysis is established through *numerically* (CFD) and the validity of performing quasi-steady analysis is established through references from the literature. The analytical steady-state models used for the PVT analysis are validated through experimental data from the literature.

5.1 Experimental validation

5.1.1 PV electrical steady state model

The five-parameter electrical model in section 2.2 is verified from experimental data reported in a study [17]. Electrical power from a building-integrated polycrystalline photovoltaic panel was experimentally measured at the National Institute of Standards and Technology (NIST) in Gaithersburg, Maryland for five sets of conditions. The specifications of the polycrystalline photovoltaic module are provided in the study [17]. Table 5.1 shows the values of electrical power obtained at maximum power point conditions for various cell temperatures and incident radiations. Measurements are taken when the cell temperature and the incident radiation have steadied after some time. There

seems to be a good agreement between the NIST values and the five-parameter model. Figure 5.1 shows the current-voltage curves of the solar cell for five sets of conditions. Figure 5.1 matches the figure provided in the study [17].

Table 5.1 Maximum electrical power measured at the NIST facility and calculated using the five-parameter model for polycrystalline silicon cell

Incident radiation [W/m^2]	Cell Temperature [˚C]	Maximum power [W/m^2]	
		NIST	Five-parameter
882.6	39.5	106.8	103.1
696	47	77.4	78.23
465.7	32.2	56.6	56.99
189.8	36.5	21.2	22.11

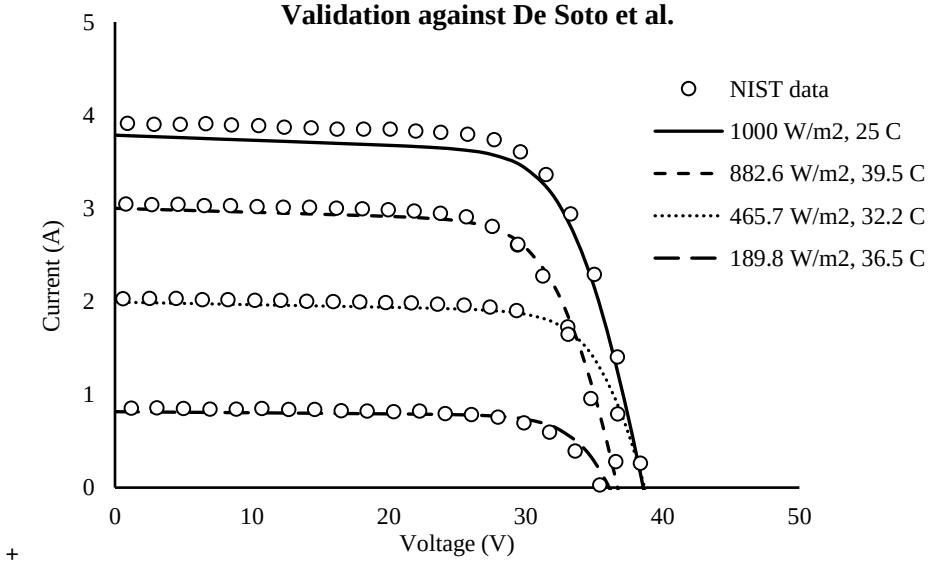

Figure 5.1 Current vs voltage for the polycrystalline cell type calculated by five-parameter model

5.1.2 Collector thermal steady state model

An experimental study [74] is used to verify the thermal efficiency of the photovoltaic-thermal (PVT) system as predicted by the current one-dimensional, steady state collector thermal model. In the current model, the mass of glass, absorber, and collector has been neglected to simplify the analysis. In the study, thermal efficiency calculations were performed at the following steady state conditions: 800 W/m^2 solar radiation, 20˚C ambient temperature, 1 m/s ambient wind speed and 0.022 kg/s. m^2 mass flow rate per area of the collector. In Figure 5.2 thermal efficiency of the PVT system was plotted against the factor $((T_i-T_a)/I_T)$ where I_T is the incoming solar radiation. This figure shows good agreement with the figure in the study [74].

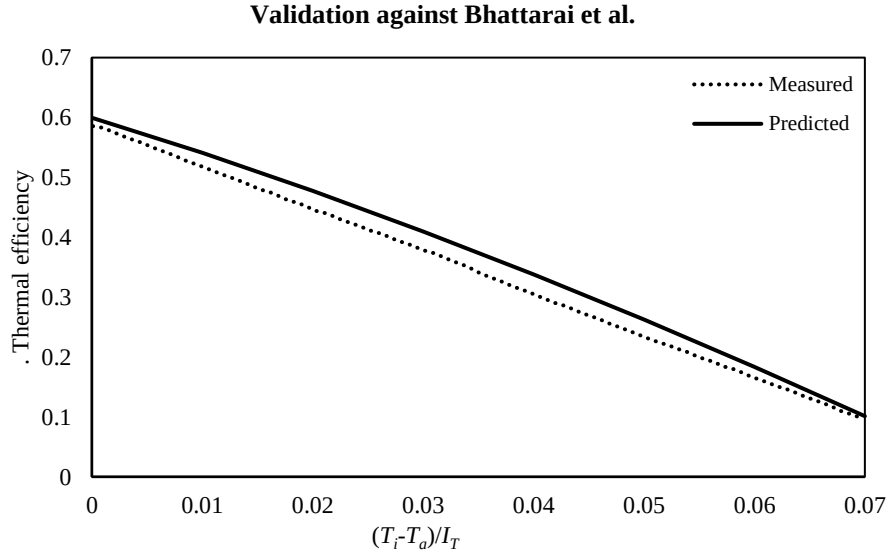

Figure 5.2 Thermal efficiency versus factor $((T_i-T_a)/I_T)$ as predicted by the thermal model

5.1.3 PVT thermal steady state model

An indoor experimental analysis was performed to investigate the cooling effect on a PV module by gluing a thermal tube-on-plate collector, which consists of an aluminum plate

absorber and two serpentine tubes, at the back of the PV module [75]. The entire module was insulated with polyurethane foam with water as the cooling fluid inside the tubes. The experimental results are listed in Table 5.2 along with the analytical results obtained using the mathematical model mentioned above. In the current model, the mass of glass, PV module, absorber, and collector has been neglected to simplify the analysis. Model results show agreement with the experimental results from the literature.

Table 5.2 Comparison of different outputs obtained by the analytical model and the experimental data

	I_T [W/m^2]	T_a [˚C]	T_i [˚C]	T_o [˚C]	T_{fluid} [˚C]	Q_u [W/m^2]	$T_{p,rear}$ [˚C]	$T_{cell,rear}$ [˚C]	T_{cell} [˚C]
Model	400	20	24.5	26.70	25.60	174.0	30.10	47.10	47.93
Experimental	400	20	24.5	26.34	25.42	147.7	24.34	49.44	49.80

5.2 Numerical validation

5.2.1 Design of PVT collector using Computational Fluid Dynamics

The thermal model in section 2.5 can only be used for one-dimensional (z-axis) thermal analysis of PVT collector. The aim of conducting CFD simulations in this study is to prove the validity of performing a one-dimensional analysis of the collector by designing and selecting a collector configuration which would give a uniform temperature distribution across the absorber plate (independent of x and y-axes) with minimum pressure drop. Additionally, temperature gradients on the collector surface can affect its electrical efficiency because solar cells operating at higher temperatures generate less power. Hence

it is necessary to use a collector configuration which would give a uniform temperature distribution.

The two most popular collector configuration found in the literature are the header-riser collector and the serpentine collector, with each configuration having its own advantages and disadvantages. In some cases the serpentine collector resulted in a superior thermal performance than header-riser collector [25], on the other hand, numerical simulations show that the header-riser collector gives better performance than serpentine collector [31].

Numerical simulation was performed on a header-riser collector design from literature [41] as shown in Figure 5.3 using water as heat transfer fluid. Simulations were performed using ANSYS FLUENT 14.5 to determine the temperature distribution on the absorber plate and the pressure distribution in the collector pipe carrying heat transfer fluid. From Figure 5.4 and Figure 5.5 it can be seen that while the pressure drop is low for the header-riser collector (pipes are in parallel hence only the pressure drop across a single pipe is relevant), the absorber plate lacks uniformity in temperature, which means that a significant temperature gradient would exist between the solar cells on either side of the plate along its length.

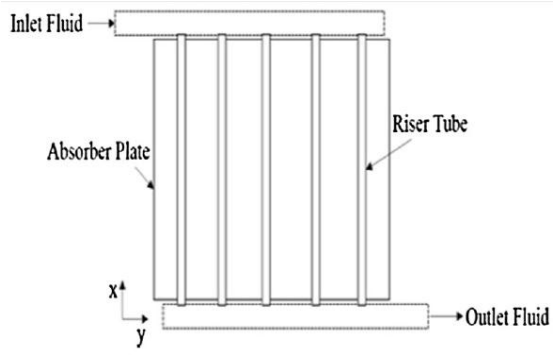

Figure 5.3 Header-riser collector schematic

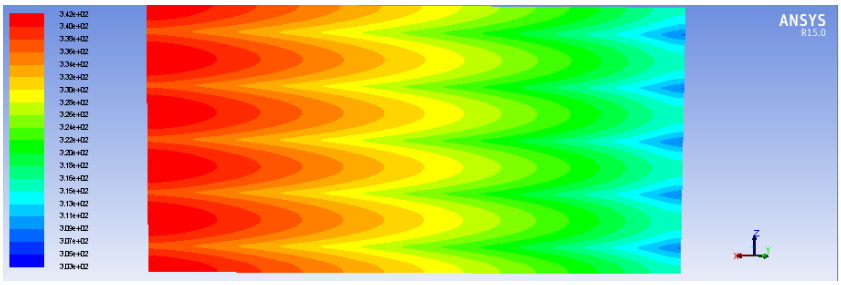

Figure 5.4 Temperature distribution across absorber plate for header-riser collector

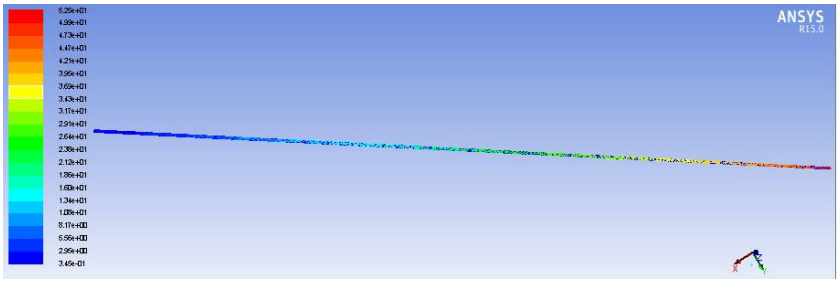

Figure 5.5 Pressure distribution across a single riser pipe for header-riser collector

Numerical simulation was performed on a serpentine collector design from literature [57] as shown in Figure 5.6 using water as heat transfer fluid. From Figure 5.7 and Figure 5.8 it can be seen that although there exists uniformity in temperature across the absorber plate for serpentine collector configuration, the pressure drop for the serpentine collector is considerably higher than a header-riser collector since all the fluid is flowing through a single tube which accumulates a lot of pressure drop due to friction, coupled with the fact that the design consists of a tube with a rectangular cross-section (rectangular cross-section pipes result in more pressure drop as compare to circular tube).

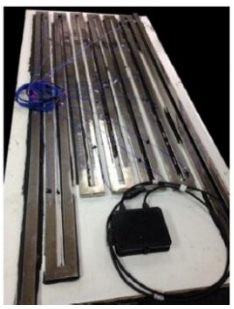

Figure 5.6 Serpentine collector schematic

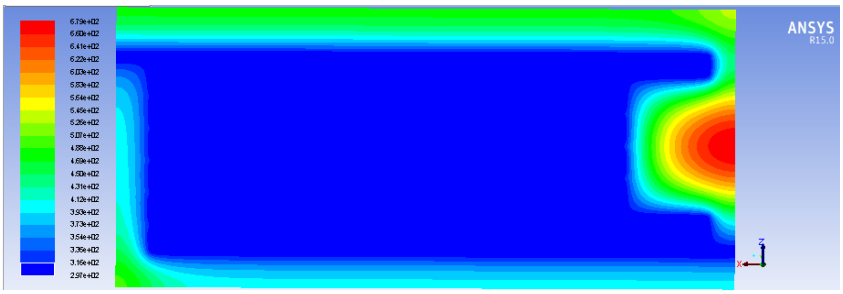

Figure 5.7 Temperature distribution across absorber plate for serpentine collector

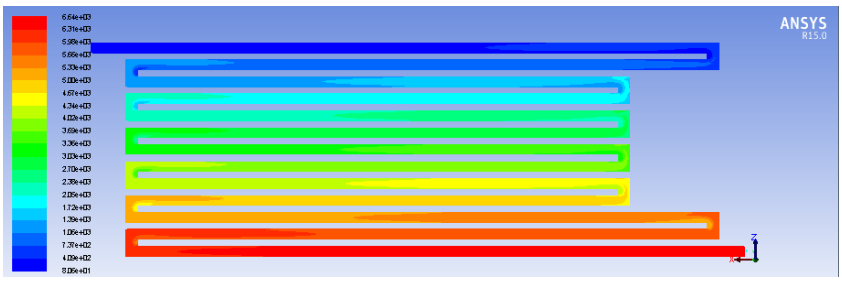

Figure 5.8 Pressure distribution across collector tube for serpentine collector

A third design suggested by Al-Shamani [33] is a hybrid of serpentine and header-riser configurations. This design is like the serpentine configuration, only instead of a single serpentine tube, there are multiple hairpin tubes beneath the absorber with two header pipes at one end. Another modification to the previous serpentine design was the use of modified tube cross-section [31] (as shown in Figure 5.10) instead of the rectangular tube cross-section. Numerical simulation was performed on this design using water as the heat transfer fluid with Figure 5.11 and Figure 5.12 showing the temperature distribution across the

absorber plate and pressure distribution across the collector tubes respectively. An advantage of this design over the serpentine configuration is that it splits the flow into 6 parts hence it reduces the pressure drop to one-sixth of that of the serpentine configuration while still maintaining the uniform temperature distribution across the absorber plate. Hence this design has been selected for the present study.

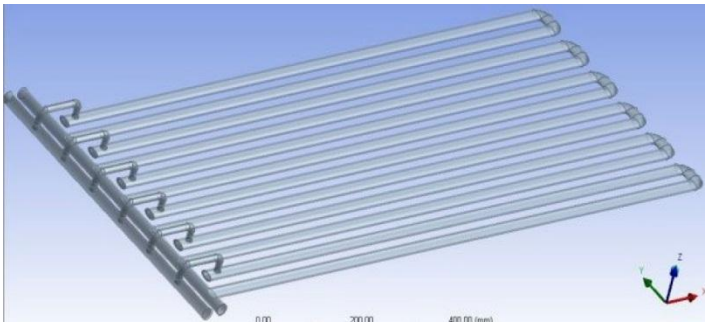

Figure 5.9 Hybrid design suggested by Al-Shamani [33]

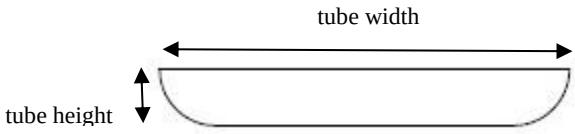

Figure 5.10 Modified tube cross-section [31]

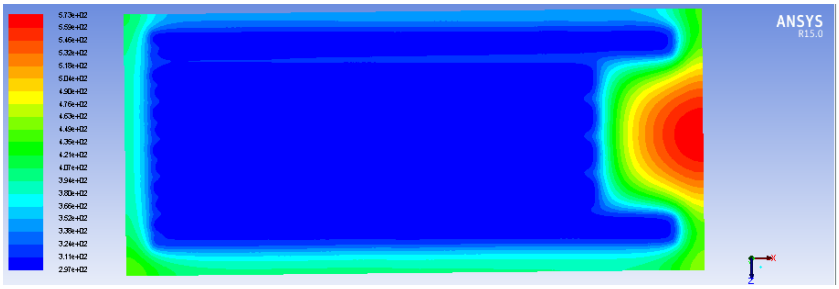

Figure 5.11 Temperature distribution across absorber plate for hybrid design

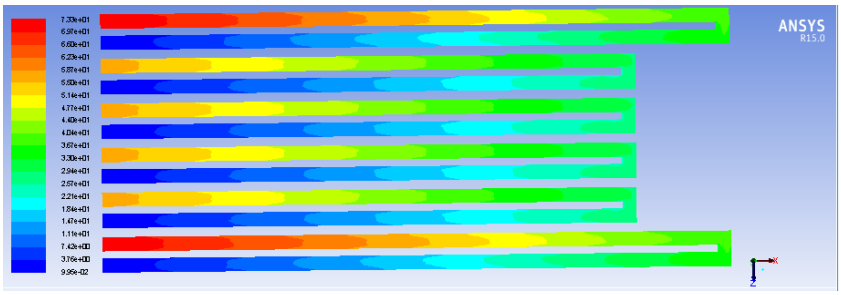

Figure 5.12 Pressure distribution across collector tube for hybrid design

CFD simulations show that the hybrid design results in a uniform temperature distribution across the absorber plate which is independent of x and y-axes. Hence the cell temperature across the PV panel can also be assumed as uniform in case of perfect thermal contact between PV and absorber plate.

5.3 Justification for quasi-steady state assumption

- The experimental meteorological data available for this study was a medium temporal resolution (Ambient conditions were constant for one hour). Hence the time step for the fluctuations in the inlet conditions, Δt_s, is limited to one hour.
- The dynamic behavior of a PVT system can be defined in terms of *time constant*, Δt_c [69]. The time constant is defined as the time required for a fluid leaving a collector to change through 63.2 % $(1 - 1/e = 0.632)$ of the total temperature change from its initial to its ultimate steady value after a step change in incident radiation or inlet fluid temperature. Δt_c of a PVT collector can be measured experimentally by studying the response of the collector to a step variation in solar irradiance.
- Experimental studies show that Δt_c of a PVT collector, like the one used in this study, ranges from 88 seconds (experimental) [76] to 138 seconds (numerical) [77].

- The response of quasi-steady state simulations will deviate significantly from results of equivalent fully dynamic simulations of the same system with the same inputs if the following condition is fulfilled [77]:

$$\Delta t_s < \frac{\Delta t_c}{2} \tag{5.3.1}$$

- Since Δt_s in this study is 3600 seconds which is much larger than the Δt_c, obtained from the literature, the use of a quasi-steady model is justified.

CHAPTER 6

RESULTS AND DISCUSSION

6.1 Performance of uncooled PV system

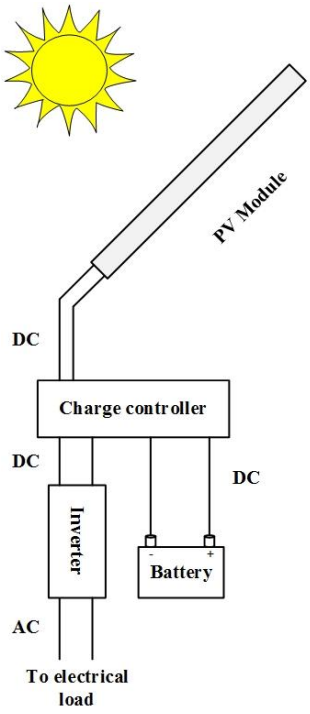

Figure 6.1 Schematic of uncooled PV system

For the uncooled PV system shown in Figure 6.1, output can be shown on a daily or monthly basis. Figure 6.2 shows the hourly variation of cell temperature and exergy efficiency of the PV panel from 07 00 AM to 04 00 PM for 16 February and from 07 00 AM to 04 00 PM for 16 August. The PV panel temperatures are higher for the hotter month (August) with temperatures reaching up to 56 ˚C. Higher cell temperatures lead to the deterioration of the electrical performance of the solar cell which results in greater exergy destruction and lower exergy efficiencies, hence exergy efficiencies are lower for August.

In contrast to August, February has lower PV panel temperatures due to low ambient temperatures, with the cell temperature reaching as low as 15.5 ˚C, without any cooling. Low cell temperatures result in improved electrical and exergy performance of the solar panel.

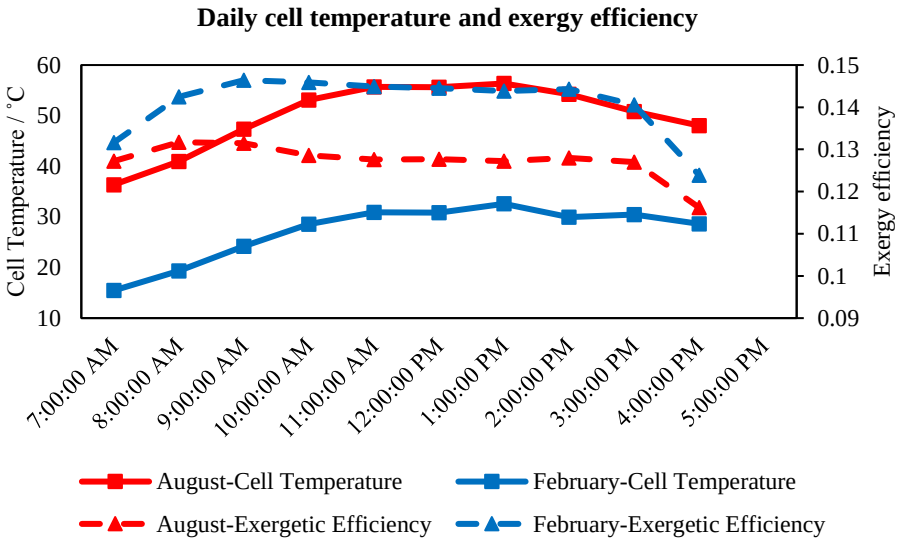

Figure 6.2 Variation in hourly cell temperature and exergy efficiency for 16 February and 16 August

Figure 6.3 shows the variation of monthly electrical power generated by the PV panel and the overall electrical efficiency of the panel. A maximum electrical power of 1.65 kW/day is achieved in March, whereas peak electrical efficiency of 13.2% is achieved in February. The hot ambient temperatures in August result in a minimum electrical efficiency of 11.7 %, however lowest electrical power is generated in January due to low incident radiation levels.

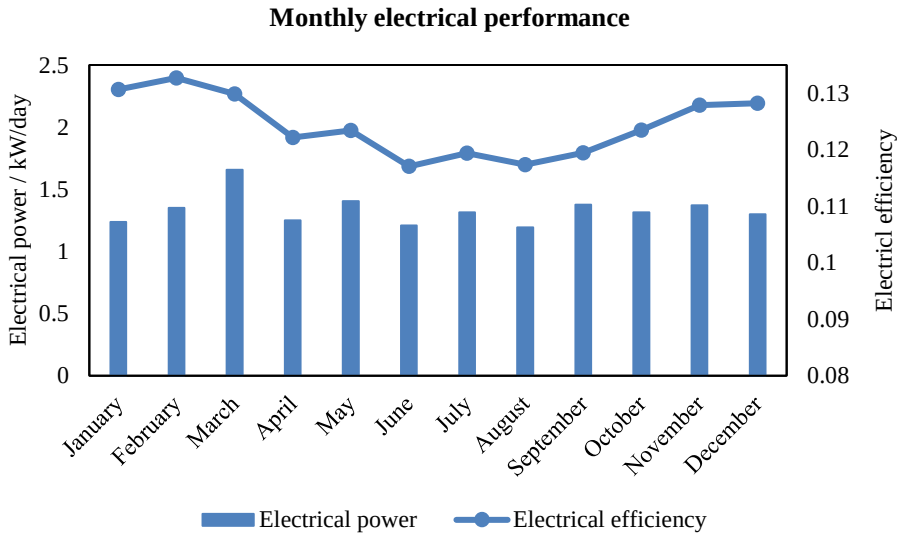

Figure 6.3 Variation in monthly electrical output and electrical efficiency of the PV panel

6.2 Performance of water-cooled PVT system

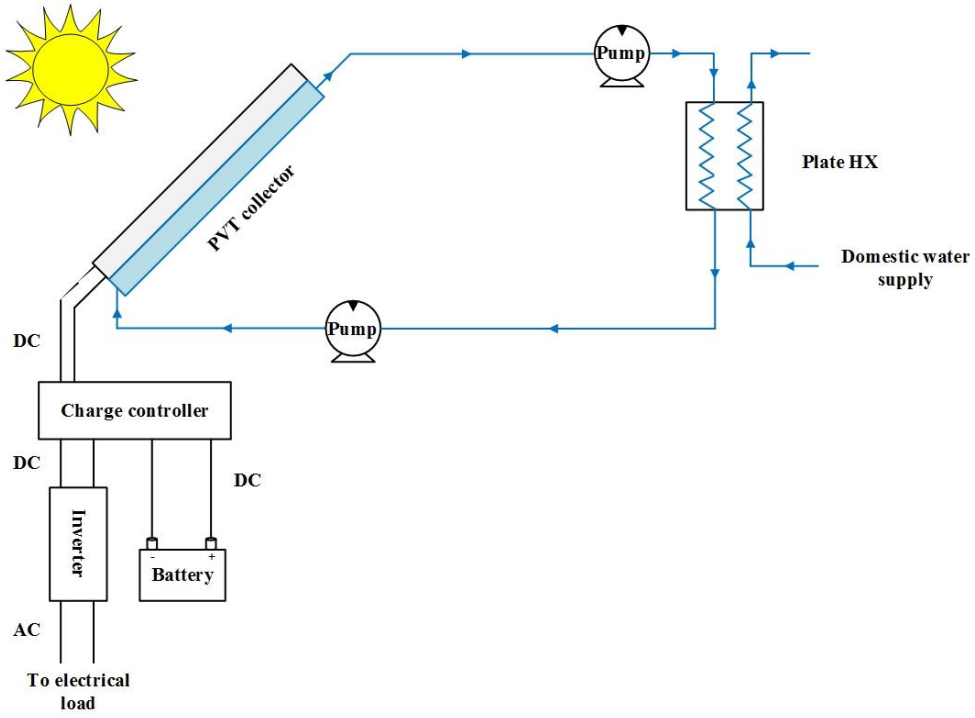

Figure 6.4 Schematic of water-cooled PVT system

The performance of water-cooled PVT system, as shown in Figure 6.4, has been analyzed with reference to the uncooled PV system. Water at a flow rate of 0.0784 kg/s was used to remove heat from the collector and was cooled with water at 0.1045 kg/s in the plate heat exchanger. Figure 6.5 shows the hourly variation in the solar cell temperature for 16 February and 16 August from 07 00 AM to 04 00 PM for uncooled PV system and water-cooled PVT system. Water cooling affects the solar cell temperature more in the summer month (August) than in the winter month (February), with the cell temperature being brought down from 56 to 33 ˚C (a temperature difference of 23 ˚C) in August. Cooling the PV panel in winter month (February) results in a maximum temperature decrease of 8 ˚C (from 33 ˚C to 24 ˚C), which is nevertheless significant. Water cooling results in an average decrease of 19 ˚C in August and an average decrease of 6.7 ˚C in February in the solar cell temperatures.

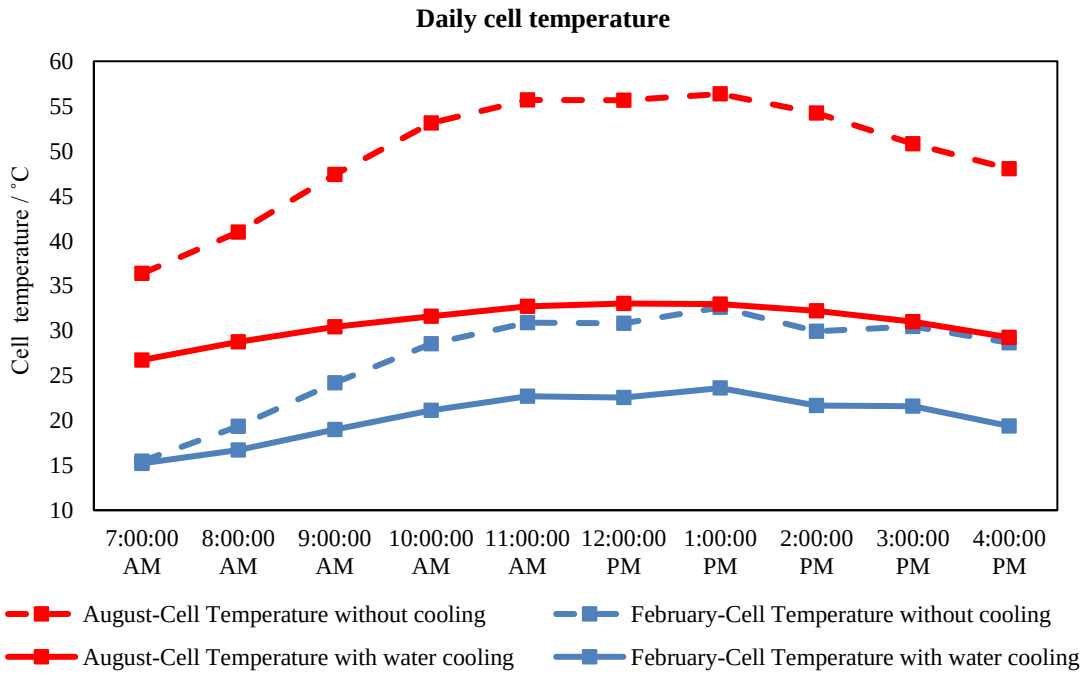

Figure 6.5 Variation in hourly cell temperature for 16 February and 16 August

Figure 6.6 shows the hourly variation in the exergy efficiency of the uncooled PV system and the water-cooled PVT system for 16 February and 16 August from 07 00 AM to 04 00 PM. The exergy efficiencies of PVT system are significantly higher than those of PV system. This is because the incident radiation is only being converted to electrical energy in PV system but it is being converted to both electrical and thermal energy in PVT system. There is better utilization and less wastage of available energy in PVT system, hence it's exergy efficiency is much higher. Higher incident radiation levels in August results in higher energy output (electrical and thermal), hence exergy efficiencies are higher in August than February.

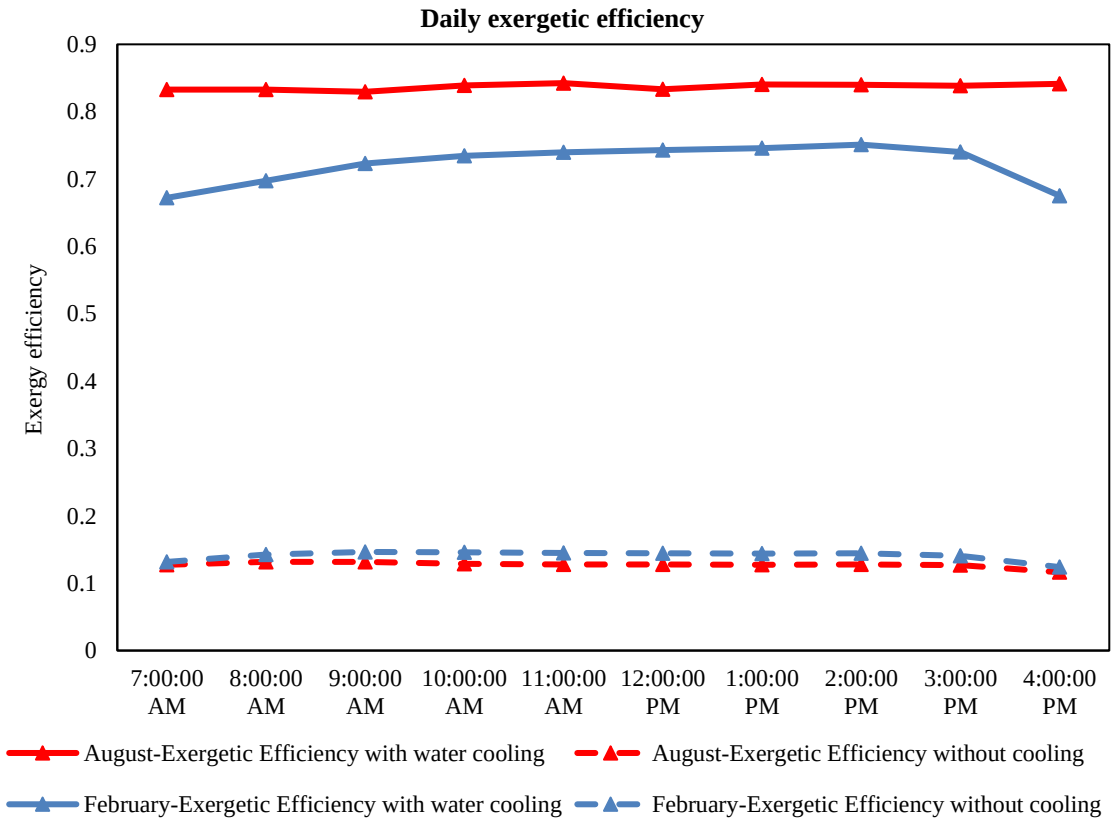

Figure 6.6 Variation in hourly exergy efficiency for 16 February and 16 August

Water cooling of PV panels results in the decrease of the overall cell temperature, which leads to an improvement in the electrical performance of the solar cell. Figure 6.7 shows the variation in the increase of electrical power resulting from PV water cooling as well as the average electrical efficiencies for uncooled PV system and water-cooled PVT system for each month. For the winter months of February and March, ambient temperatures are already low, so there is no significant improvement in the electrical performance. August show the largest increase in the electrical power of 12.2 %, along with the highest increase in the average electrical efficiency from 11.5 to 12.9 %.

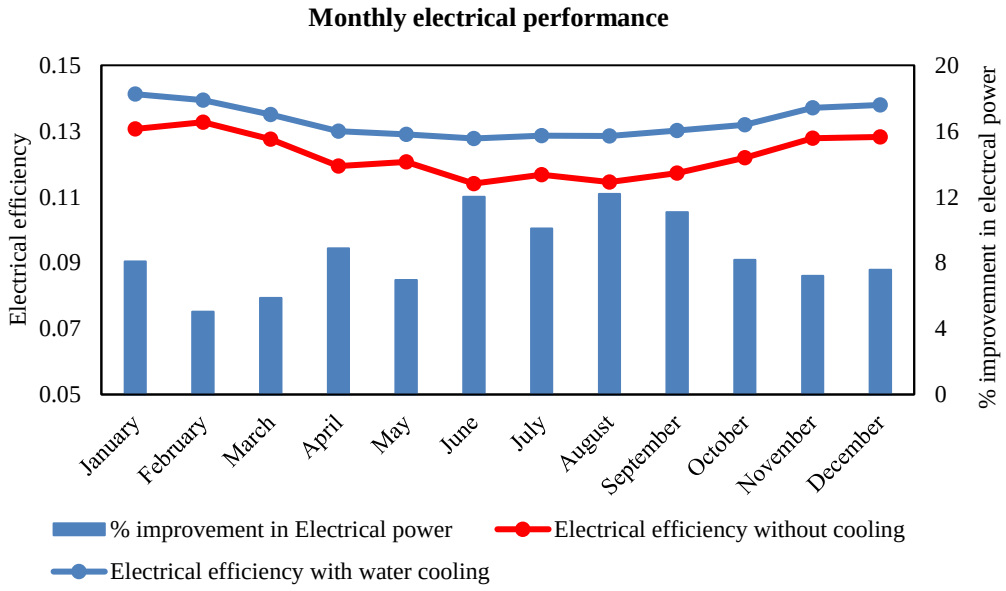

Figure 6.7 Variation in monthly electrical efficiency and % improvement in the electrical output of PV panel

Thermal power refers to the energy gained by the heat transfer fluid in the collector of the PVT system. As per Figure 6.8 a maximum thermal power of 6.75 kW/day is achieved in September, whereas peak thermal efficiency of 62.2 % is achieved in June.

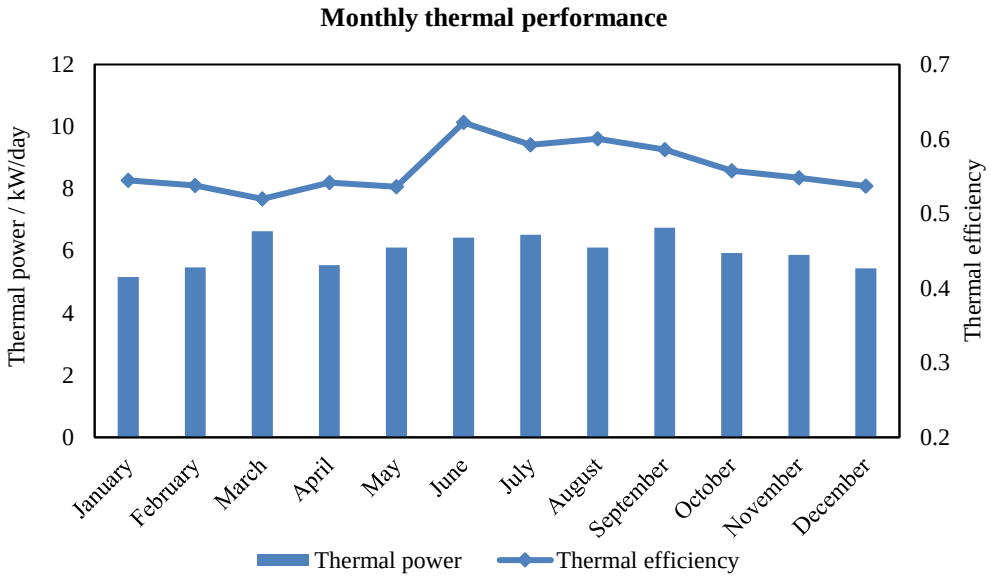

Figure 6.8 Variation in monthly thermal output and thermal efficiency of the water-cooled PVT system

6.3 Performance of silver/water nanofluid-cooled PVT system

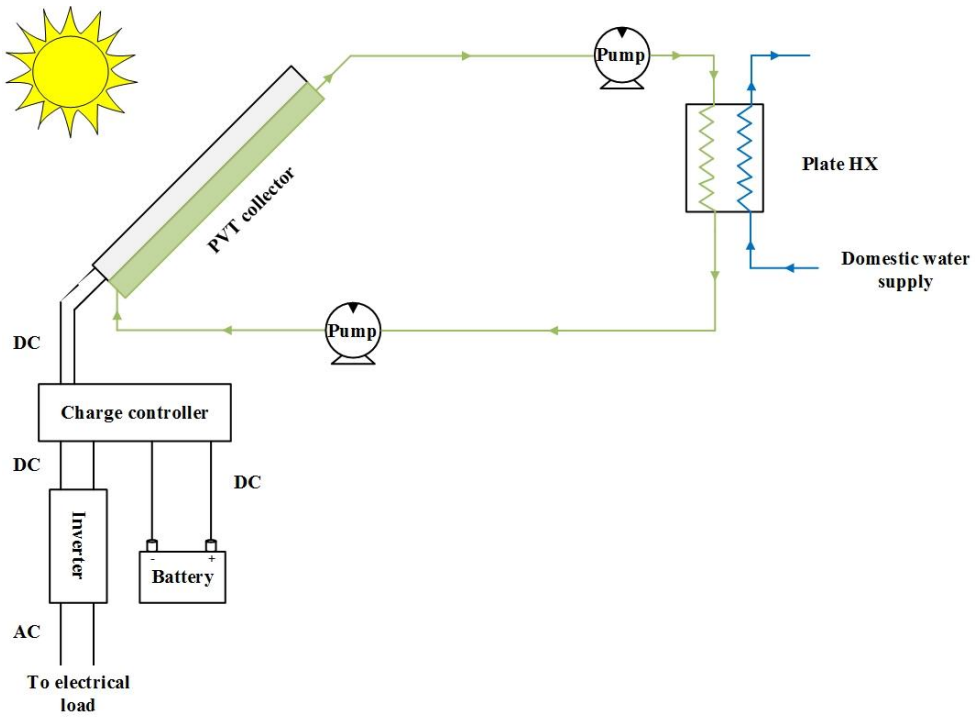

Figure 6.9 Schematic of nanofluid-cooled PVT system

Figure 6.9 shows the schematic of nanofluid-cooled PVT system. The heat transfer fluid in the collector (water) as replaced with silver/water nanofluid at a nanoparticle concentration of 0.5 vol% having nanoparticles at an average size of 10 nm. Nanofluid at a flow rate of 0.0784 kg/s was used to remove heat from the collector and was cooled with water at 0.1045 kg/s in the plate heat exchanger. The performance of nanofluid-cooled PVT system has been analyzed with reference to the water-cooled PVT system. Figure 6.10 shows the hourly variation in the solar cell temperature for 16 February and 16 August from 07 00 AM to 04 00 PM for the water-cooled PVT system and the nanofluid-cooled PVT system. A maximum of 1.5˚C and 1 ˚C temperature decrease is achieved in August and February respectively, using nanofluid over water as the heat transfer fluid in the PVT collector.

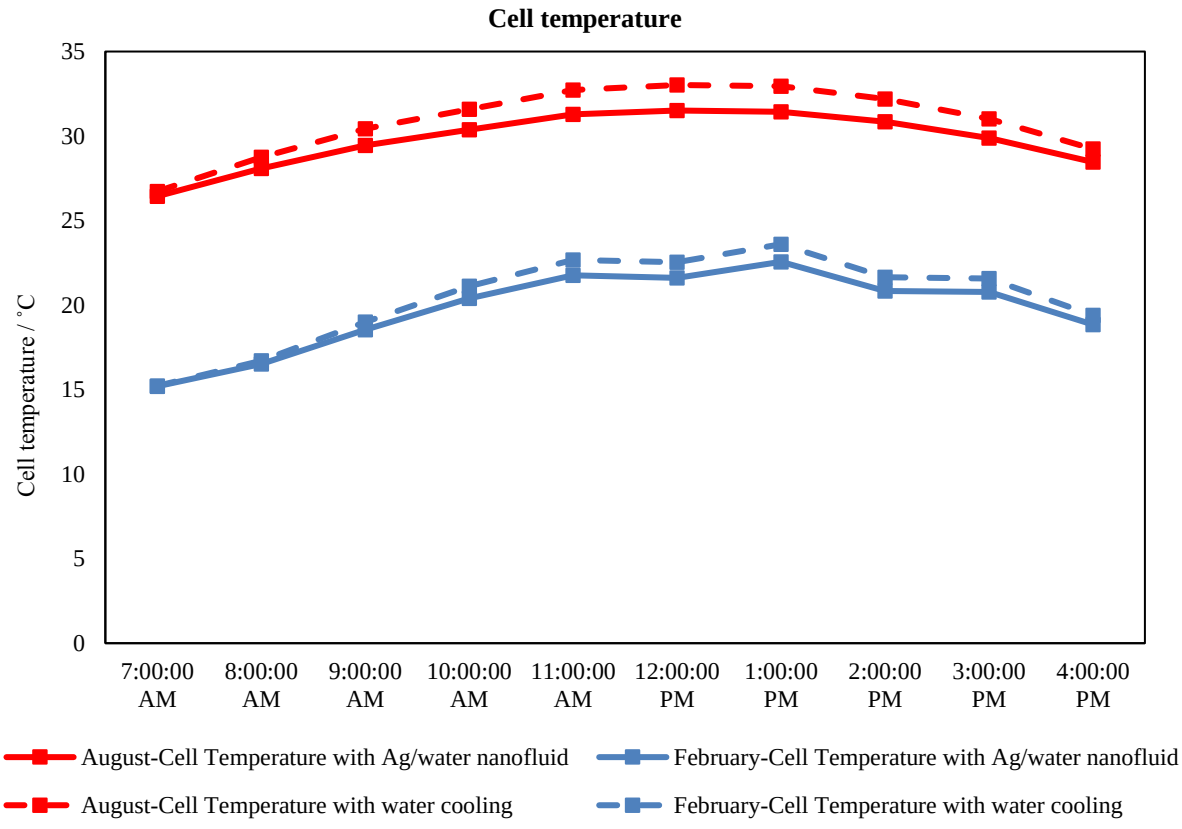

Figure 6.10 Variation in hourly cell temperature for 16 February and 16 August

Figure 6.11 and Figure 6.12 show the electrical and thermal performance of the water-cooled PVT and the nanofluid-cooled PVT system for each month. The introduction of silver/water nanofluid to the system had a marginal effect on both electrical and thermal performance of the system. A maximum of 0.7 % improvement in the electrical output was observed relative to water-cooled PVT system in September and a maximum of 1.4 % improvement in the thermal output was achieved in September through silver/water nanofluid.

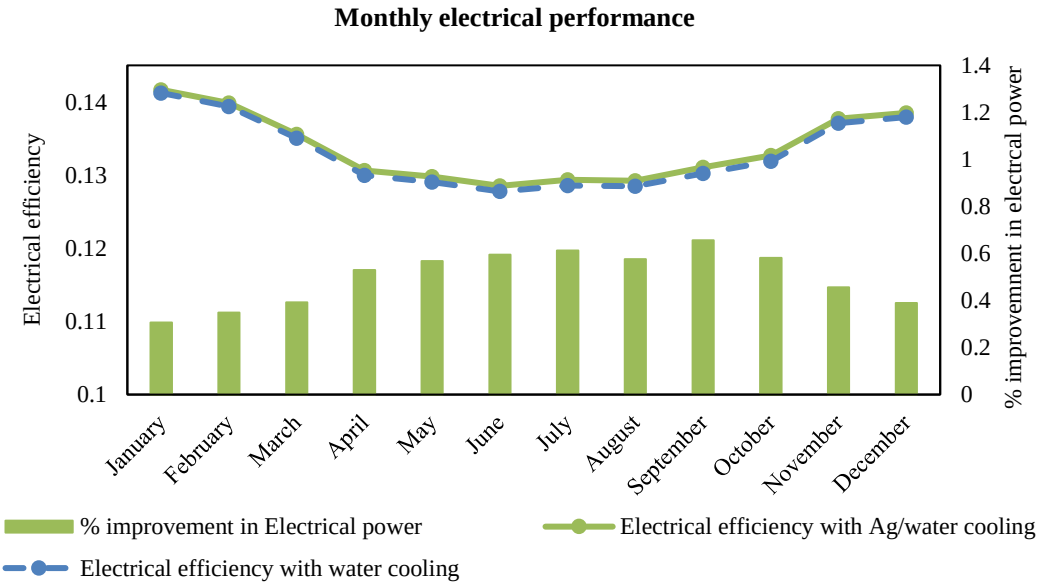

Figure 6.11 Variation in monthly electrical efficiency and % improvement in the electrical output of PV panel

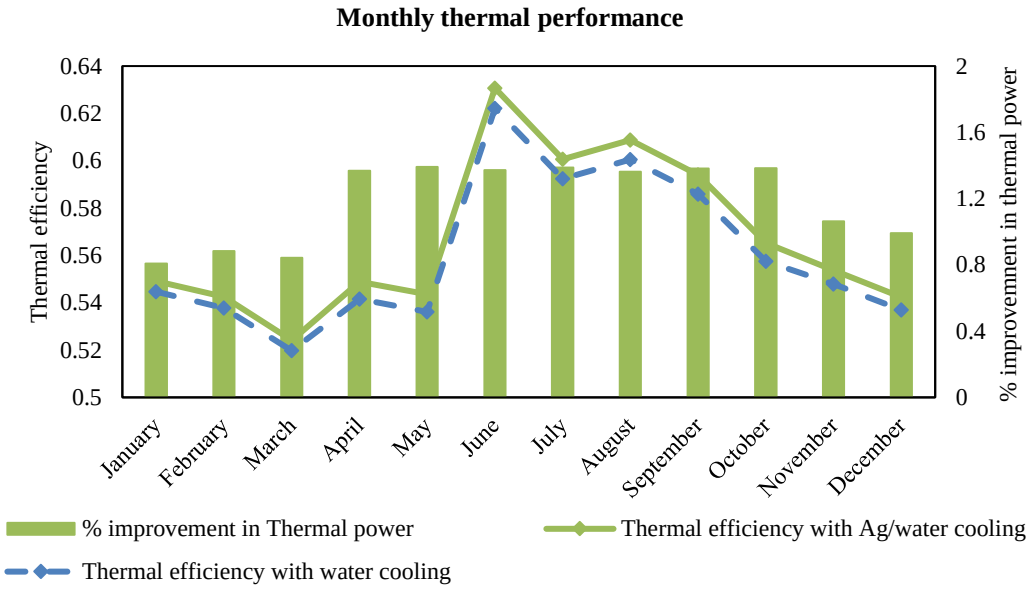

Figure 6.12 Variation in monthly thermal efficiency and % improvement in the thermal output of PV panel

6.4 Performance of silver/water nanofluid-cooled PVT system with PCM-Thermal battery

The schematics for nanofluid-cooled PVT system with PCM-Thermal battery during sunlight hours and dark hours are shown in Figure 3.1 and Figure 3.2 respectively. The previous design was updated with the inclusion of a PCM-Thermal battery to store thermal energy which would be used to cover a portion of the thermal load. Nanofluid at a flow rate of 0.078 kg/s was used to remove heat from the collector and was cooled by the thermal battery which housed PCM at a temperature of 28 ˚C. The performance of nanofluid-cooled PVT system with PCM-Thermal battery has been analyzed with reference to the nanofluid-cooled PVT system. Figure 6.14 shows the hourly variation in the solar cell temperature for 16 February and 16 August from 07 00 AM to 04 00 PM for the nanofluid-cooled PVT system with and without PCM-Thermal battery. As predicted, the inclusion of PCM-Thermal battery with a melting point of 28 ˚C has raised cell temperatures in both months.

A maximum of 2.7˚C and 12.6˚C temperature rise is observed in August and February respectively, with the use of PCM-Thermal battery. Increase in cell temperature is higher in February (winter month) than August (summer month) because in February, cell temperatures are already lower due to colder ambient conditions. For both months, the final cell temperatures approach the same values because of the isothermal nature of PCM.

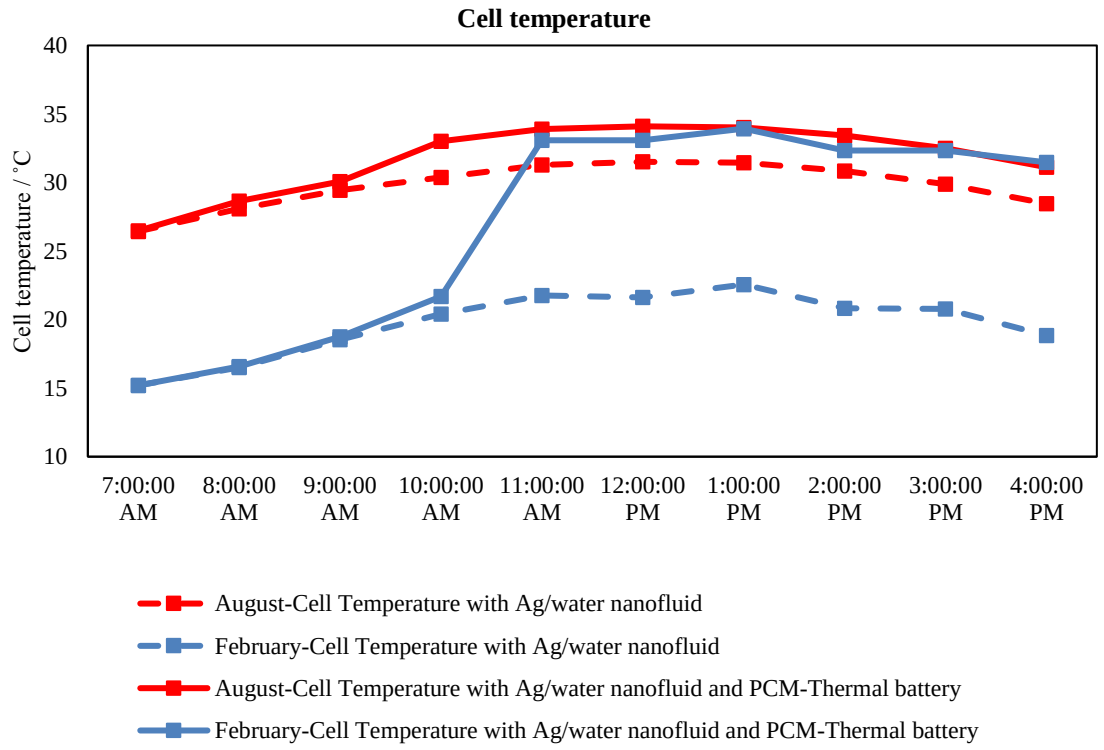

Figure 6.13 Variation in hourly cell temperature for 16 February and 16 August

Figure 6.15 and Figure 6.16 show the electrical and thermal performance of the water-cooled PVT and the nanofluid-cooled PVT system for each month. The introduction of PCM-Thermal battery to the system has resulted in a maximum reduction of 5.1 % in the electrical output in March and a maximum reduction of 12.4 % in the thermal output in January.

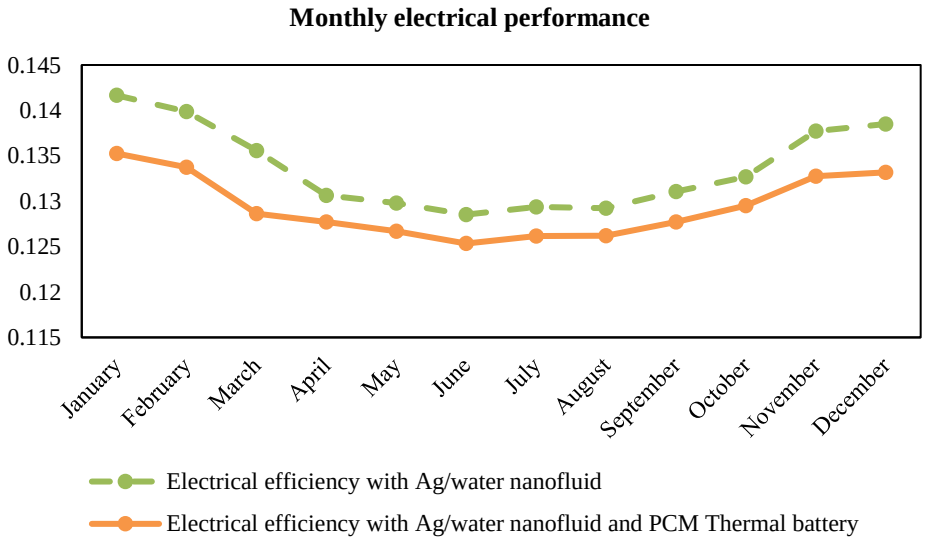

Figure 6.14 Effect of thermal battery on the monthly electrical efficiency of PV panel

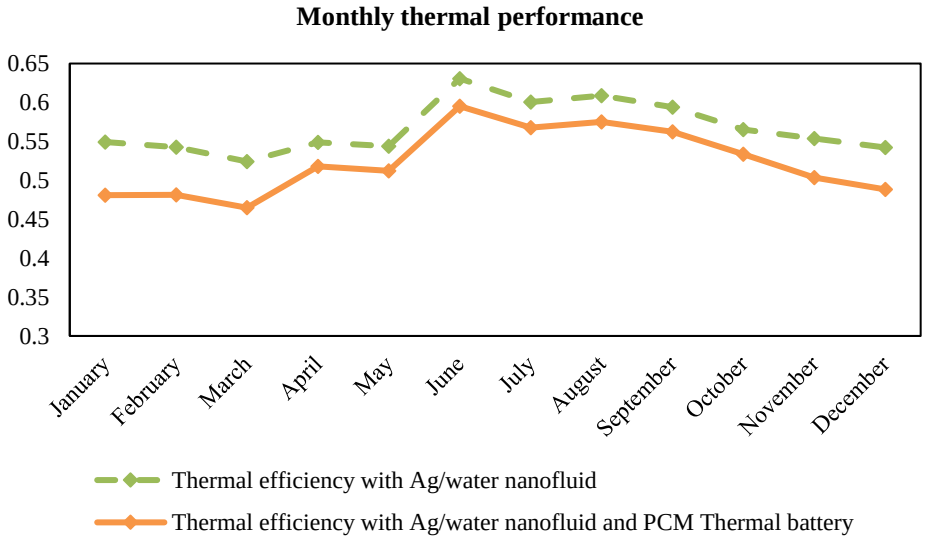

Figure 6.15 Variation in monthly thermal efficiency and % improvement in the thermal output of PV panel

Since the solar cell considered in this study is a polycrystalline silicon PV module, it cannot cover the entire electrical load because of its limited electrical efficiency. Figure 6.17 shows the variation in the monthly percentage of electrical load satisfied by solar. A maximum of 77 % of electrical load is covered by solar in March and an average of 62%

of electrical load is covered by solar throughout the year. The remainder of required load can be covered through the electrical grid. Solar electrical fraction can be further increase by using other types of PV cells such as monocrystalline silicon, gallium arsenide or perovskite solar cells.

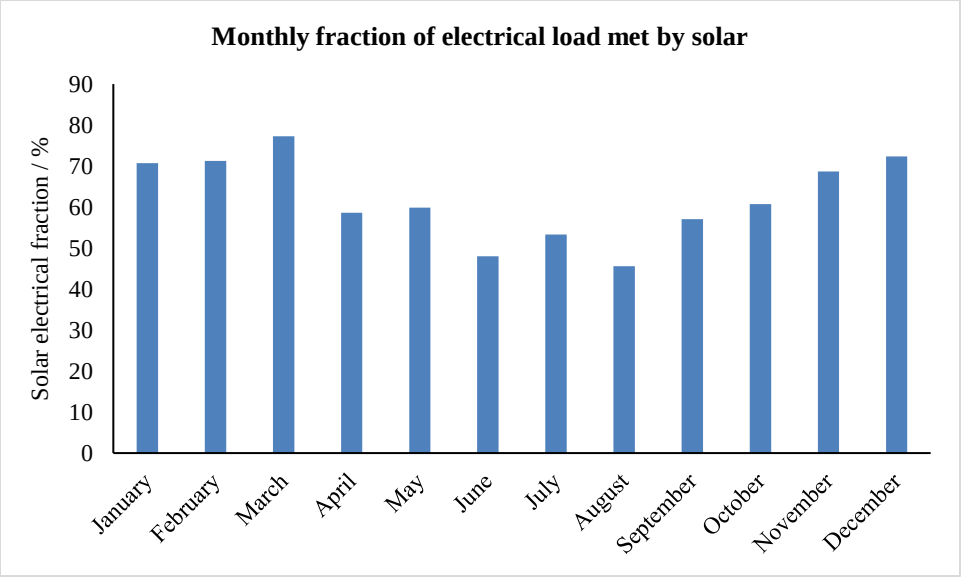

Figure 6.16 Monthly variation of percentage of electrical load covered by solar

The inclusion of PCM-thermal battery has made it possible to cover a portion of thermal load as well. Figure 6.18 shows the variation in the monthly percentage of thermal load satisfied by solar. A maximum of 27.3 % of thermal load is covered by solar in September and an average of 20.5 % of thermal load is covered by solar throughout the year.

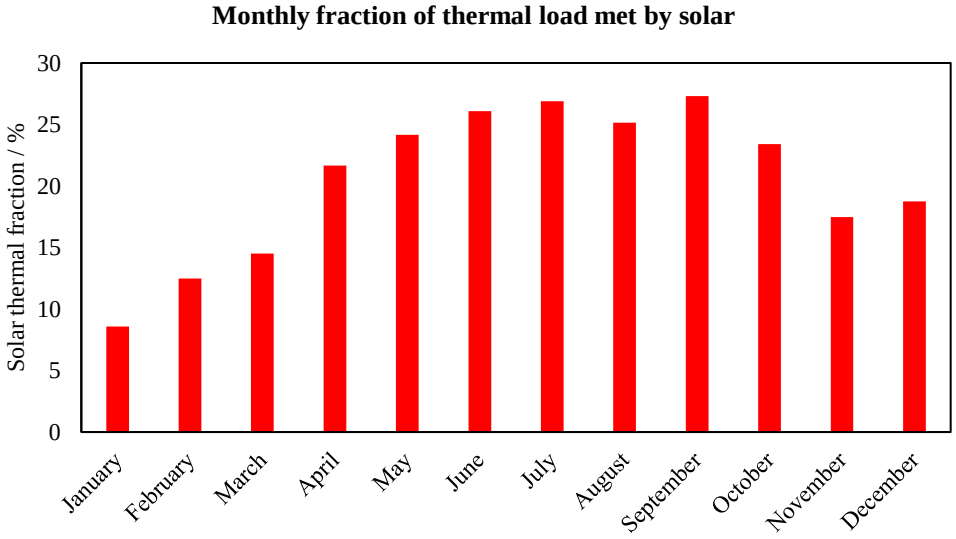

Figure 6.17 Monthly variation of percentage of thermal load covered by solar

6.5 Pressure drop and pumping power

In active PVT systems, collector fluid is pressurized and pushed through the collector and thermal battery/ heat exchanger through fluid pumps. Pressurizing the fluid also increases its velocity which enhances heat transfer in collector and thermal battery/ heat exchanger. Hence fluid pumps become are important components of PVT system and the AC electrical power consumed by pumps must be subtracted from the total AC electrical power generated by the PV panel before it is either consumed by AC electrical load during light hours or stored in DC electric battery to cover the AC electrical load during dark hours.

At any time, only two of the three pumps are operational. The maximum total pressure drop experienced by the PVT system used in this study is calculated using the analytical model in section 4.8. The maximum total pressure drop is calculated to be **7125 Pa** or pressure head of 2.38 m. Hence, the pump must supply a flow rate of 180 L/h and overcome a pressure head of 2.38 m.

The **SOBO WP-3400** pump supplies a maximum flow rate of 880 L/h along with a head of 1.2 m and consumes electrical power of 15 W. Since the actual pressure head is almost twice, **two** such pumps must be used with power input requirement of **30 W**.

Figure 6.18 SOBO WP-3400 submersible pump

6.6 Battery and inverter sizing

The size of the electrical battery would depend on the maximum amount of excess energy that can be stored throughout the year. Since most electrical power is produced in March (Figure 6.17), only the daily electricity generated profile of March is used along with the electrical load profile when determining the excess energy available as shown in Figure 6.20. Since solar energy is only available during the day, excess electrical energy generated from 10 00 AM to 03 00 PM must be conserved using an electrical battery so that it can be used at night (05 00 PM to 12 00 PM).

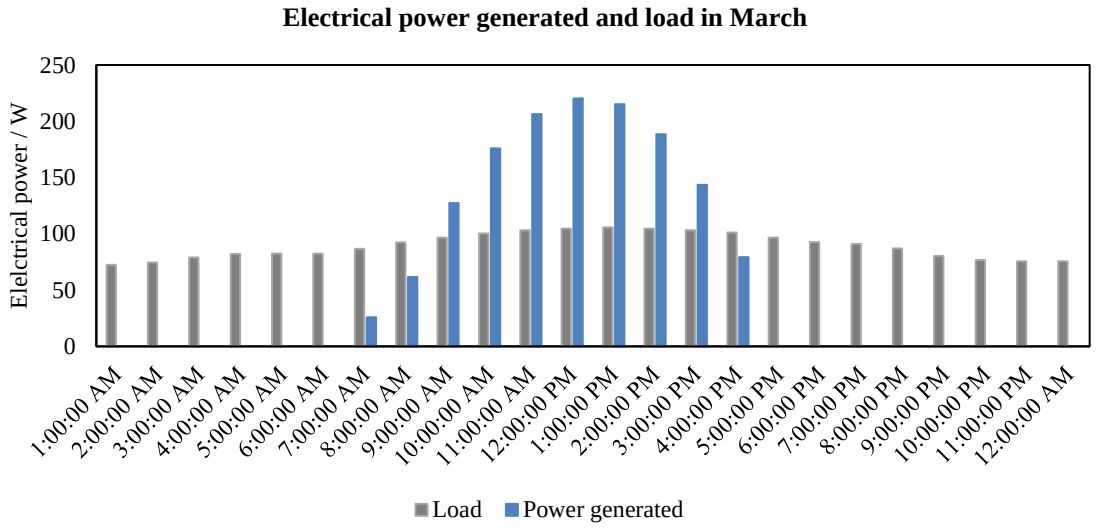

Figure 6.19 Variation of hourly electrical energy generated in March and the daily electrical load

The maximum excess electrical energy which can be saved is **559 W.h.** Assuming the voltage of the system to be 12 VDC, the battery capacity can be calculated

$$Battery\ capacity = \frac{Excess\ energy}{System\ voltage * Battery\ efficiency} = \frac{559\ W.h}{0.85 * 12\ V} = 55\ A.h$$

The **SLA: Sealed Lead Acid Battery 12V 55 A.h** is suitable for this system.

Figure 6.20 SLA 12V-55 Ah lead acid battery

For the inverter sizing, only the peak excess power and system voltage are required. The peak excess power is **116 W** at 12 00 PM in March, so the inverter rated power is:

$$Rated\ power = \frac{Peak\ energy}{Power\ factor * inverter\ efficiency} = \frac{116\ W}{0.8 * 0.9} = 161\ W$$

The **BELTT 350 W 12 VDC** power inverter is suitable for this system.

Figure 6.21 BELTT 350 W 12 VDC power inverter

6.7 Economic analysis

Initially, the total initial investment cost, *IC* is determined by summing up the present costs of all the components in the system. Most of these costs were obtained through the website: alibaba.com. Table 6.1 shows the breakdown of the *IC*:

Table 6.1 Investment cost breakdown

Component	**Price [US$]**
PV panel	85
Inverter	10
Battery	43

Charge controller	30
Pump	16.66
Heat exchanger	319
PVT collector	90
Nanofluid	45.84
Thermal battery	398
Piping	19.26
Installation	30.59
Total investment cost	**1087.35**

The total investment cost is calculated to be **US$ 1087.35**. The total annual maintenance cost, *MC* is determined using the assumption mentioned in section

$$MC = 2.76\ \%\ of\ PV\ cost + 2.3\ \%\ of\ Heat\ exchanger\ cost + 0.75\ \%\ of\ pump\ cost$$
$$= US\$\ 9.81$$

The total maintenance cost is calculated to be **US$ 9.81**. The total annual replacement cost, *RC* consists of the annual sum of the cost of components replaced over the lifetime of the system. Since the system has a life of 20 years and the battery and inverter are to be replaced at every 7 months, replacement costs amounting to **US$ 53** would only be incurred at year 7 and 14. Information which is specific to the region of interest i.e. Saudi Arabia such as the domestic electricity price, COE_i, domestic electricity inflation rate, i_{EC}, and inflation

rate and i_e and discount rate, i_d has been obtained from multiple websites. The analysis period or the life of the plant is chosen to be 20 years.

Considering the data in Table 6.2, the **simple cost payback time** can be calculated as:

$$CPBT = \frac{IC}{EC_L * COE_i} = \frac{1124.35}{4201.935 * 0.0133} = \mathbf{5.231\ years}$$

The *LCC* or the life cycle cost is **US$ 1403**. The ALCC and COE can now be calculated as follow:

$$ALCC = LCC \times CRF = 369 * 0.06116 = \boldsymbol{US\$\ 85.83}$$

$$COE = \frac{ALCC}{EC_L} = \frac{22.57}{4201.935} = \boldsymbol{US\$\ 0.005505\ per\ kW/hr}$$

The cost of energy generated by PVT is **58.71 %** less than the current domestic electricity price.

Table 6.2 Key parameters for economic analysis

Replacement period for battery and inverter		7 years
Total investment cost	*IC*	US$ 1087.35
Capital recovery factor	*CRF*	0.06116
Annual electricity saved for electrical load	EC_L	4129.685 kW.hr
Annual electricity saved for thermal load	EC_H	11460.385 kW.hr
Total annual electricity saved per year	$EC_{sav\ per\ year}$	15590.07 kW.hr

Annual maintenance cost	MC	US$ 9.81
Annual replacement cost	RC	US$ 50
Domestic cost of electricity	COE_i	0.0133 US$ / kW.hr
Domestic electricity inflation rate	i_{EC}	4.4 %
Inflation rate	i_e	2.69 %
Annual electrical PV system performance degradation rate	D_L	1 %
Annual water heating performance degradation rate	D_H	1.5 %
Discount rate	i_d	2 %
Life of system	np	20 years

Figure 6.22 shows the annual variation of discounted cash flow for year Y, DCF_y throughout the 20-year life of the system. The two sharp decreases in DCF_y for year 7 and 14 is due to the replacement of battery and inverter in these years which reduces the net incoming cash flow.

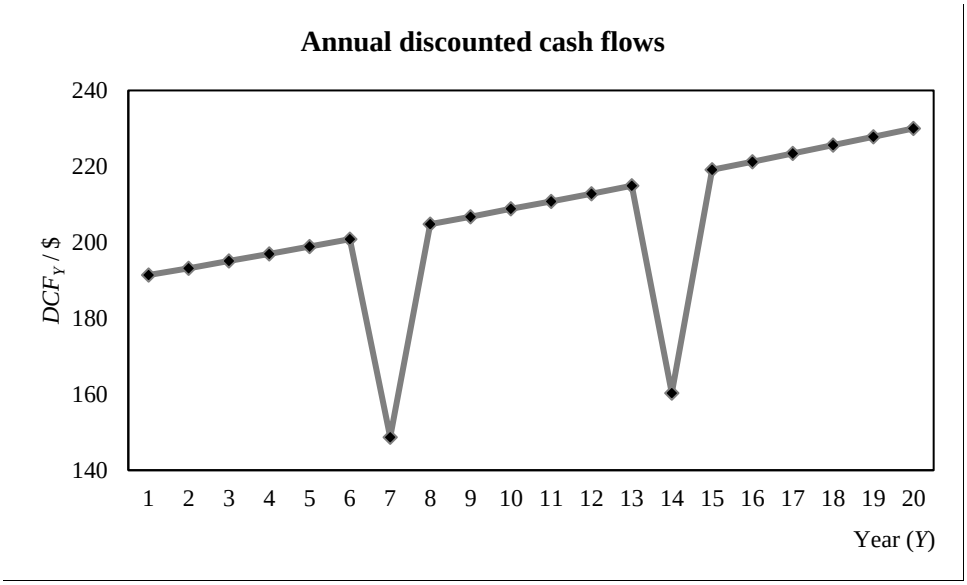

Figure 6.22 Discounted cash flow for Y year throughout the 20-year life of system

Figure 6.23 shows the annual variation of life cycle cost for year *Y*, LCC_y throughout the 20-year life of the system. LCC_y changes from negative to positive at the time between 5th and 6th year, thus indicating that the **discounted cost payback time** is **5.5 years**.

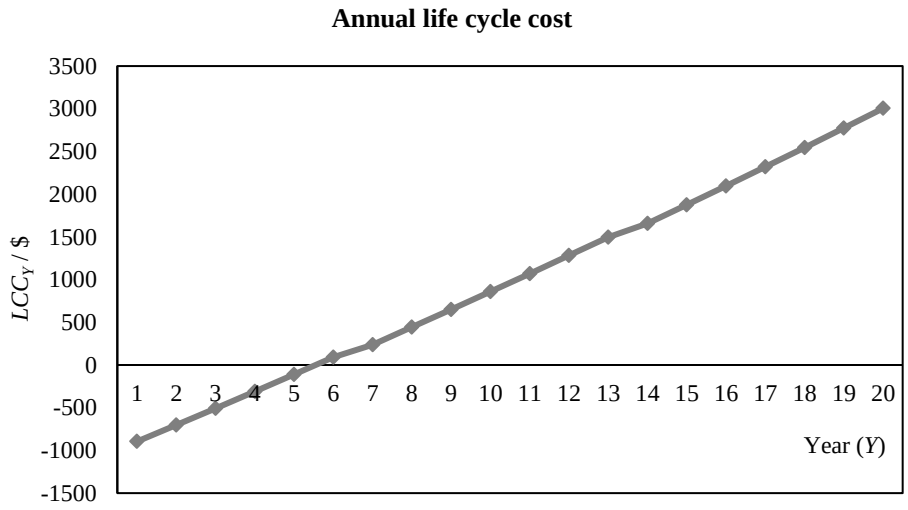

Figure 6.23 Life cycle cost of *Y* year throughout the 20-year life of system

Figure 6.24 shows the effect of varying discount rate on the life cycle cost of the system for year 20. The curve meets the horizontal axis at a discount rate of ***19.7 %***. This is also

the ***internal rate of return*** (IRR) of the system. Since the current discount rate is 2 %, this means that investment in this system is economically feasible.

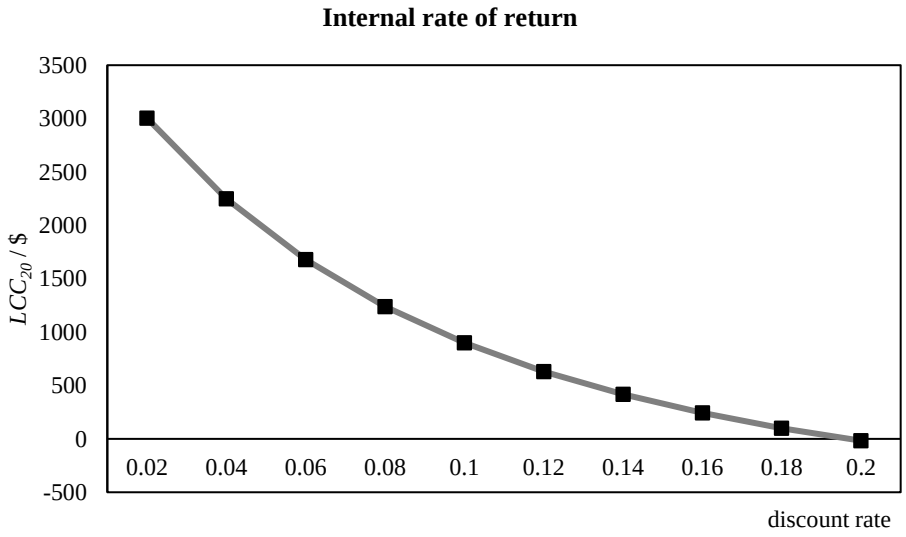

Figure 6.24 Discount rate sensitivity analysis for PVT system

From an environmental point of view, this system could prevent the emission of ***10,195.91 tons of CO_2*** into the atmosphere (considering the emission factor of Saudi Arabia to be 0.654 tCO_2/kW.hr [78])

6.8 Chapter summary

The major findings of the present study can be summarized as:

- Uncooled PV system's performance was better for winter month with temperatures as low as 15.5 ˚C. However, the performance worsened for summer month (August) with temperature as high as 56 ˚C and the resulting dip in electrical efficiency to up to 11.7 %.

- Water cooling of PV panel through the hybrid collector shown in Figure 3.4 resulted in a reduction of 23 ˚C in cell temperature and an improvement of 12.2 % in the electrical output for the summer month of August.
- Silver/water nanofluid cooling of PV panel through the same hybrid collector resulted in a reduction of 25˚C in cell temperature and an improvement of 12.8 % in the electrical output for the summer month of August.
- The preceding design is updated with inclusion of a PCM-Thermal battery to cover a portion of thermal load which results in a reduction of 22˚C in cell temperature and an improvement of 11.7 % in the electrical output for the summer month of August.
- The updated PVT system can cover 77 % of the electrical load in March and 27.3 % of the thermal load in September.
- The capital investment cost of the updated design is estimated to be US$ 1087.35 and, considering the annual economic benefits of the proposed system the payback period of the system is calculated to be 5.5 years.
- The cost of energy of proposed system is 58.7 % lower than the domestic electricity price in Saudi Arabia and the system has the potential to prevent the release of 10,195.91 tons of CO_2 into the atmosphere.

CHAPTER 7

CONCLUSIONS AND RECOMMENDATIONS

Conclusions

Considering the rapid increase in population and the consequent expansion of domestic infrastructure in Saudi Arabia, a photovoltaic/thermal system is designed to meet a portion of the electrical and thermal energy needs of a residential building through solar energy. Nanofluid is used as an alternative to the conventional collector fluid i.e. water and computational fluid dynamics was used to select the best possible thermal collector configuration. A PCM-Thermal battery was included in design to account for the temporal mismatch in the thermal energy supply and demand profiles. For a hybrid, parallel-serpentine collector design, results show a maximum of 11.7 % improvement in the electrical output of nanofluid-cooled PVT system with PCM-Thermal battery over uncooled PV system. Furthermore, an economic analysis was conducted to determine the monetary benefits of the system which shows that the cost of energy from proposed system is 58.7 % less than the domestic energy price, and the entire initial investment is estimated to be recovered at the end of 5.5 years. The system could also prevent the release of 10,195.91 tons of CO_2 into the atmosphere.

Recommendations

Due to the complex nature of phase-change process, a detailed three-dimensional transient CFD modelling is needed to analyze the performance of PCM-Thermal battery.

Appendix A. Dhahran meteorological data 2014

Table A.1 Meteorological data for Dhahran for *n* days of 2014

	January			**February**		
Hour	**Incident Radiation**	**Ambient Temp.**	**Wind Speed**	**Incident Radiation**	**Ambient Temp.**	**Wind Speed**
	W/m^2	**˚C**	**m/s**	**W/m^2**	**˚C**	**m/s**
7:00 AM	16.41	12.86	4.571	29.64	15	4.322
8:00 AM	175.4	12.45	4.386	206.7	15.74	3.86
9:00 AM	381.6	14.62	1.953	427.6	17.15	5.429
10:00 AM	550.1	17.05	1.94	616	18.33	5.725
11:00 AM	659.2	17.68	2.994	751	19.26	7.099
12:00 PM	694.8	18.41	2.436	736.7	20.02	7.818
1:00 PM	671.8	19.89	1.684	811	20.41	8.14
2:00 PM	564.5	20.76	1.251	620.5	20.97	8.58
3:00 PM	417.6	20.05	3.262	579.6	21.62	9.32
4:00 PM	253.9	19.2	3.661	364.2	21.93	8.3
	March			**April**		
7:00 AM	121.6	13.49	6.59	182.3	24.87	2.585
8:00 AM	372.6	14.11	7.066	363.8	26.35	2.741
9:00 AM	610.4	15.49	6.318	585	28.65	1.851
10:00 AM	797.4	16.9	5.824	794.9	30.98	1.582
11:00 AM	923	18.29	6.248	864	32.69	1.509
12:00 PM	982	19.4	6.716	843	34.05	1.484

1:00 PM	961	20.6	6.797	801	34.41	2.14
2:00 PM	851	21.85	6.223	720.9	32.3	4.112
3:00 PM	681.3	21.58	6.431	580.2	31.95	4.046
4:00 PM	472.6	20.73	7.073	414.4	30.9	4.25
	May			**June**		
7:00 AM	306.8	26.76	4.415	277.5	36.26	7.042
8:00 AM	558	28.18	4.899	500.5	37.61	5.67
9:00 AM	750.3	29.73	4.341	676.8	40.12	6.018
10:00 AM	876	31.27	4.336	798.1	42.04	6.871
11:00 AM	921	32.36	3.647	861	43.95	7.376
12:00 PM	929	32.83	3.982	864	44.93	6.007
1:00 PM	917	32.7	5.511	835	45.18	6.798
2:00 PM	836	32.36	6.328	776.5	45.26	6.663
3:00 PM	690.2	32.08	5.639	670.6	44.52	7.664
4:00 PM	506.4	31.41	6.48	502	44.04	7.091
5:00 PM	290.2	30.82	4.656	301.4	43.07	6.997
	July			**August**		
7:00 AM	233.2	34.48	8.17	156.2	34	4.189
8:00 AM	461.6	35.58	8.25	412.8	35.05	4.727
9:00 AM	659.4	36.96	7.312	590.7	37.14	2.906
10:00 AM	821	38.27	7.636	701	39.68	2.203
11:00 AM	935	39.43	7.347	815	41.51	2.956
12:00 PM	971	41.29	7.136	851	40.97	3.043

1:00 PM	946	41.34	6.806	837	41.53	2.774
2:00 PM	862	40.84	6.97	762.1	40.65	2.639
3:00 PM	721.8	40.67	6.427	647.5	39.98	2.987
4:00 PM	532	38.69	5.217	468.3	40.41	2.874
5:00 PM	313.3	38.44	3.797			
	September			**October**		
7:00 AM	178	31.55	4.222	116.1	27.9	2.2
8:00 AM	422.5	33.24	3.54	346.4	28.75	2.288
9:00 AM	633.2	35.14	3.219	550.4	30.24	2.866
10:00 AM	805	37.76	3.421	701.9	31.64	3.526
11:00 AM	892	39.07	3.312	789.3	32.37	3.503
12:00 PM	907	39.99	3.113	805	33.28	3.189
1:00 PM	879	40.2	4.641	756.1	33.68	3.815
2:00 PM	783.6	39.58	5.215	653.8	33.51	4.245
3:00 PM	603.6	38.96	4.189	495.6	34.33	2.803
4:00 PM	396.5	37.73	4.293	282.4	33.33	3.707
	November			**December**		
7:00 AM	69.52	22.04	2.226	32.54	18.5	2.274
8:00 AM	278	23.16	1.498	216.4	19.07	1.79
9:00 AM	489.3	23.99	1.894	415	20.08	1.499
10:00 AM	651.7	24.98	1.952	572.3	20.46	1.922
11:00 AM	754	25.31	4.039	672.1	21.09	1.67
12:00 PM	781.3	25.61	4.329	701.4	22.59	1.626

1:00 PM	723.6	25.7	3.835	668.4	23.46	2.805
2:00 PM	599.1	25.63	3.808	570.1	24.05	2.635
3:00 PM	427.4	25.53	3.381	411.5	24.52	2.571
4:00 PM	218.3	25.16	2.74	204.8	24.25	3.331

Appendix B. Daily electrical load profile

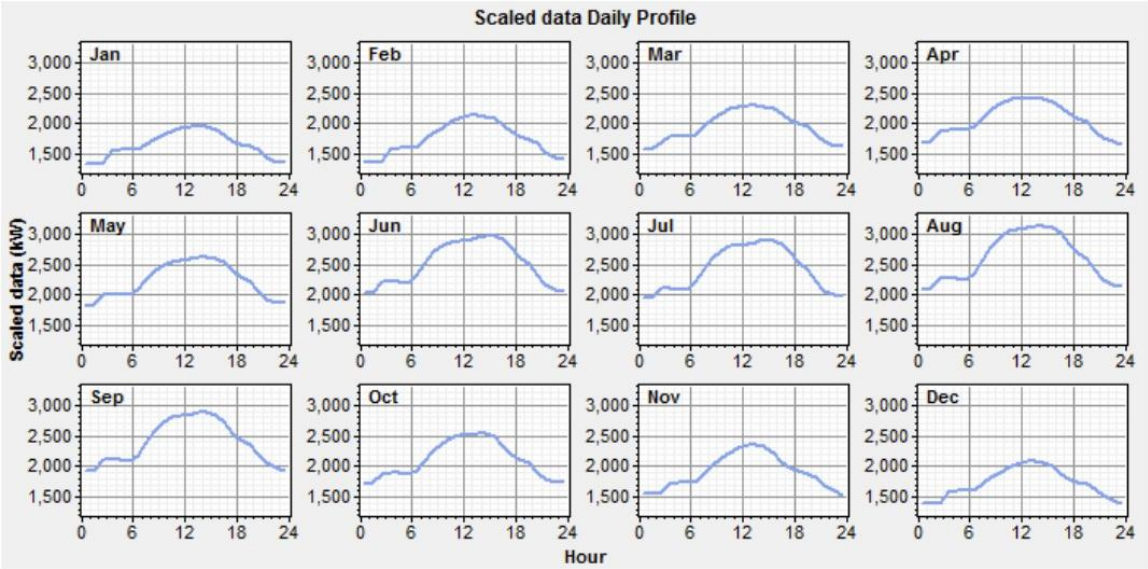

Figure B.1 Variation of hourly electricity consumption for a residential building in Yanbu, Saudi Arabia [66]

Appendix C. Daily hot water load profile

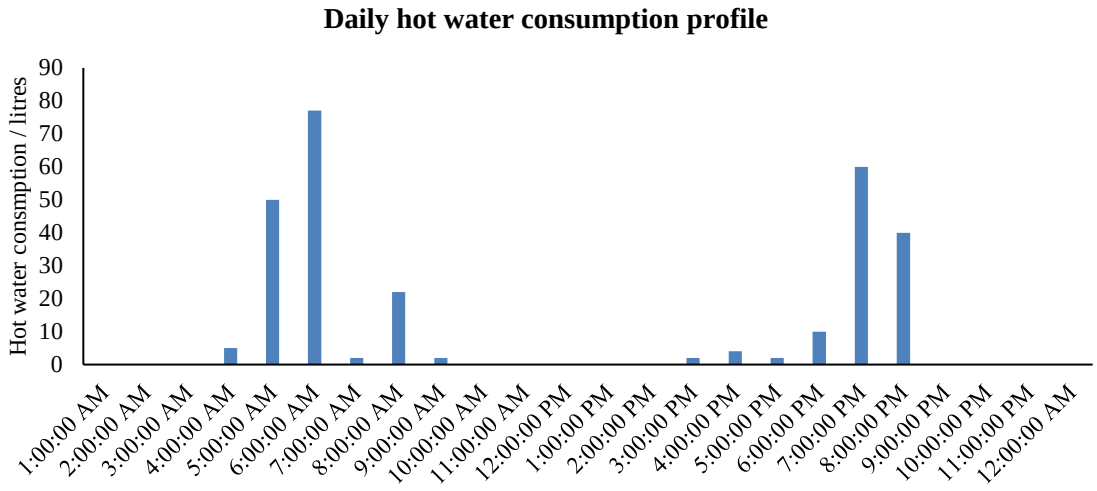

Figure C.1 Variation of hourly hot water consumption for a residential building in the UK [67]

Appendix D. Declination angle

Table D.1 Recommended Average Days for Months [69]

Month	Date	Number of day of year/*n*	Declination angle/ δ
January	17	17	-20.9
February	16	47	-13.0
March	16	75	-2.4
April	15	105	9.4
May	15	135	18.8

June	11	162	23.1
July	17	198	21.2
August	16	228	13.5
September	15	258	2.2
October	15	288	-9.6
November	14	318	-18.9
December	10	344	-23.0

Appendix E. Five-parameter electrical model for solar cell

[17,69]

Initially, values are determined for reference conditions i.e. 25 ˚C and 1000 W/m^2

$$a_{ref} = \frac{1.025\ k_b\ T_{c,ref}\ N_s}{q} \tag{0.1}$$

where k_b is the Boltzmann constant and q is the elementary charge constant and $T_{c,ref}$ is 298 K (25 ˚C).

The four equations below are simultaneously solved for $I_{L,\,ref}$, $I_{o,\,ref}$, $R_{s,\,ref}$ and $R_{sh,\,ref}$, whereas, $a_{\,ref}$, $I_{mp,\,ref}$ $V_{mp,\,ref}$ are known.

$$I_{sc,ref} = I_{L,ref} - I_{o,ref}\left[e^{\frac{I_{sc,ref}R_{s,ref}}{a_{ref}}} - 1\right] - \frac{I_{sc,ref}R_{s,ref}}{R_{sh,ref}} \tag{0.2}$$

$$I_{L,ref} = I_{o,ref}\left[e^{\frac{V_{oc,ref}}{a_{ref}}} - 1\right] - \frac{V_{oc,ref}}{R_{sh,ref}} \tag{0.3}$$

$$I_{mp,ref} = I_{L,ref} - I_{o,ref}\left[e^{\frac{V_{mp,ref} + I_{mp,ref}R_{s,ref}}{a_{ref}}} - 1\right] + \frac{V_{mp,ref} + I_{mp,ref}R_{s,ref}}{R_{sh,ref}} \tag{0.4}$$

$$\frac{I_{mp,ref}}{V_{mp,ref}} = \frac{\frac{I_{o,ref}}{a_{ref}}\left[e^{\frac{V_{mp,ref} + I_{mp,ref}R_{s,ref}}{a_{ref}}}\right] + \frac{1}{R_{sh,ref}}}{1 + \frac{I_{o,ref}R_{s,ref}}{a_{ref}}\left[e^{\frac{V_{mp,ref} + I_{mp,ref}R_{s,ref}}{a_{ref}}}\right] + \frac{R_{s,ref}}{R_{sh,ref}}} \tag{0.5}$$

The values determined at reference conditions are substituted in the following set of equations to determine the output values at cell temperature (T_c) and absorbed radiation (S)

$$\mu_{Voc} = \frac{V_{oc} - V_{oc,ref}}{T_c - T_{c,ref}} \tag{0.6}$$

$$\frac{a}{a_{ref}} = \frac{T_c}{T_{c,ref}} \tag{0.7}$$

$$\frac{I}{I_{o,ref}} = \left(\frac{T_c}{T_{c,ref}}\right)^3 e^{\left(\frac{E_{g,ref}}{kT_{c,ref}} - \frac{E_g}{kT_c}\right)} \tag{0.8}$$

$$\frac{E}{E_{g,ref}} = 1 - C\left(T_c - T_{c,ref}\right) \tag{0.9}$$

where $E_{g,ref}$ =1.794*10-19 J and C =0.0002677 for silicon

$$I_L = \frac{S}{S_{ref}}\left[I_{L,ref} + \mu_{Isc}\left(T_c - T_{c,ref}\right)\right] \tag{0.10}$$

$$\frac{R_{sh}}{R_{sh,ref}} = \frac{S_{ref}}{S} \tag{0.11}$$

$$I_{mp} = I_L - I_o\left[e^{\frac{V_{mp}+I_{mp}R_s}{a}} - 1\right] + \frac{V_{mp} + I_{mp}R_s}{R_{sh}} \tag{0.12}$$

$$\frac{I_{mp}}{V_{mp}} = \frac{\frac{I_o}{a}\left[e^{\frac{V_{mp}+I_{mp}R_s}{a}}\right] + \frac{1}{R_{sh}}}{1 + \frac{I_oR_s}{a}\left[e^{\frac{V_{mp}+I_{mp}R_s}{a}}\right] + \frac{R_s}{R_{sh}}} \tag{0.13}$$

Appendix F. Vaschy-Buckingham theorem [39]

$$\pi_1 = 1.04 + {\pi_2}^{1.11}{\pi_3}^{0.33}{\pi_4}^{-1.7}\left[\frac{1}{{\pi_4}^{-1.7}} - \frac{262}{{\pi_3}^{0.33}} + \left(135{\pi_5}^{0.23}{\pi_6}^{0.82}{\pi_7}^{-0.1}{\pi_8}^{-7}\right)\right] \tag{0.1}$$

$$\pi_1 = \frac{k_{fluid}}{k_f} \tag{0.2}$$

$$\pi_2 = \varphi_{nf} \tag{0.3}$$

$$\pi_3 = \frac{k_n}{k_f} \tag{0.4}$$

$$\pi_4 = Pr_{fluid} \tag{0.5}$$

$$\pi_5 = \frac{d_{ref}}{d_p} \tag{0.6}$$

$$\pi_6 = \frac{\mu_f/\rho_f}{d_p v_{br}} \tag{0.7}$$

$$\pi_7 = \frac{\mu_f/\rho_f}{{T_{fluid}}^{-1}{v_{br}}^2} \tag{0.8}$$

$$\pi_8 = \frac{T_b}{T_{fluid}} \tag{0.9}$$

$$v_{br} = \sqrt{\frac{18k_bT_{fluid}}{d_p\pi\rho_n}} \tag{0.10}$$

$$Pr_{fluid} = \frac{\mu_{fluid}c_{p,fluid}}{k_{fluid}} \tag{0.11}$$

where d_{ref} is the molecular diameter of hydrogen equal to 2.9 angstroms.

Appendix G. Zhang and Lavan model [25,69]

$$F_R = F_1\,F_3\,F_5\left[\frac{2F_4}{F_6\,exp\left[\sqrt{1-{F_2}^2}/F_3\right]+F_5}-1\right] \tag{0.1}$$

$$F_1 = \frac{\kappa}{U_L W_{coll}}\frac{\kappa R(1+\gamma)^2-1-\gamma-\kappa R}{[\kappa R(1+\gamma)-1]^2-(\kappa R)^2} \tag{0.2}$$

$$F_2 = \frac{1}{\kappa R(1+\gamma)^2-1-\gamma-\kappa R} \tag{0.3}$$

$$F_3 = \frac{\dot{m}_{fluid}\,c_{p,fluid}}{F_1\,U_L\,A_c} \tag{0.4}$$

$$F_4 = \left(\frac{1-{F_2}^2}{{F_2}^2}\right)^{\frac{1}{2}} \tag{0.5}$$

$$F_5 = \frac{1}{F_2}+F_4-1 \tag{0.6}$$

$$F_6 = 1-\frac{1}{F_2}+F_4 \tag{0.7}$$

$$\kappa = \frac{(k_{abs}\delta_{abs}U_L)^{1/2}}{\sinh\left[(W_{coll} - d_o)\left(\frac{U_L}{k_{abs}\delta_{abs}}\right)^{1/2}\right]} \tag{0.8}$$

$$\gamma = -2\cosh\left[(W_{coll} - d_o)\left(\frac{U_L}{k_{abs}\delta_{abs}}\right)^{1/2}\right] - \frac{d_o\,U_L}{\kappa} \tag{0.9}$$

$$R = \frac{1}{\pi d_i\, h_{fluid}} \tag{0.10}$$

where W is the center to center distance between the riser pipes, d_o is the outer diameter of the riser pipe, d_i is the inner pipe diameter, h_{fi} is the convection heat transfer coefficient inside the pipe, δ_{abs} is the absorber plate thickness and k_{abs} are the absorber plate thermal conductivity.

References

[1] Saidur R, Leong KY, Mohammad HA. A review on applications and challenges of nanofluids. Renew Sustain Energy Rev 2011;15:1646–68. doi:10.1016/j.rser.2010.11.035.

[2] Polvongsri S, Kiatsiriroat T. Performance Analysis of Flat-Plate Solar Collector Having Silver Nanofluid as a Working Fluid. Heat Transf Eng 2014;35:1183–91. doi:10.1080/01457632.2013.870003.

[3] Hassani S, Taylor RA, Mekhilef S, Saidur R. A cascade nanofluid-based PV/T system with optimized optical and thermal properties. Energy 2016;112:963–75. doi:10.1016/j.energy.2016.06.142.

[4] KSA power consumption 3 times world average 2005. http://www.arabnews.com/news/598481 (accessed December 1, 2015).

[5] Electricity consumption per capita of Top 50 countries 2015. http://www.indexmundi.com/g/r.aspx?t=50&v=81000&l=en (accessed December 1, 2015).

[6] Electricity - The Ninth Development Plan 2015. http://www.mep.gov.sa/inetforms/themes/clasic/file/download (accessed December 1, 2015).

[7] ClearSky Advisors: Solar Achieves Grid Parity in Saudi Arabia – Significant Developments Expected 2015. http://www.clearskyadvisors.com/3207/solar-achieves-grid-parity-in-saudi-arabia-significant-developments-expected/ (accessed December 1, 2015).

[8] Radziemska E. Thermal performance of Si and GaAs based solar cells and

modules: A review. Prog Energy Combust Sci 2003;29:407–24. doi:10.1016/S0360-1285(03)00032-7.

[9] Radziemska E. The effect of temperature on the power drop in crystalline silicon solar cells. Renew Energy 2003;28:1–12.

[10] Dyk EE Van, S BJ, M EL. Temperature dependence of performance of crystalline silicon photovoltaic modules kT (I Research letters. S Afr J Sci 2000;96:198–200.

[11] Dash PK, Gupta NC, Centre SE, Complex CGO, Delhi N. Effect of Temperature on Power Output from Different Commercially available Photovoltaic Modules. J Eng Res Appl 2015;5:148–51.

[12] Kalogirou SA, Tripanagnostopoulos Y. Hybrid PV/T solar systems for domestic hot water and electricity production. Energy Convers Manag 2006;47:3368–82. doi:10.1016/j.enconman.2006.01.012.

[13] Silverman TJ, Deceglie MG, Marion B, Cowley S, Kayes B, Kurtz S. Outdoor performance of a thin-film gallium-arsenide photovoltaic module. Conf Rec IEEE Photovolt Spec Conf 2013:103–8. doi:10.1109/PVSC.2013.6744109.

[14] Fathi M, Abderrezek M, Djahli F, Ayad M. Study of Thin Film Solar Cells in High Temperature Condition. Energy Procedia 2015;74:1410–7. doi:10.1016/j.egypro.2015.07.788.

[15] Wang Z, Zhang H, Zhao W, Zhou Z, Chen M. The Effect of Concentrated Light Intensity on Temperature Coefficient of the InGaP / InGaAs / Ge Triple-Junction Solar Cell 2015:106–11.

[16] Steiner MA, Geisz JF, Friedman DJ, Olavarria WJ, Duda A, Moriarty TE. Temperature-dependent measurements of an inverted metamorphic multijunction

(IMM) solar cell. Conf Rec IEEE Photovolt Spec Conf 2011:002527–32. doi:10.1109/PVSC.2011.6186461.

[17] De Soto W, Klein SA, Beckman WA. Improvement and validation of a model for photovoltaic array performance. Sol Energy 2006;80:78–88. doi:10.1016/j.solener.2005.06.010.

[18] Segal A, Epstein M, Yogev A. Hybrid concentrated photovoltaic and thermal power conversion at different spectral bands. Sol Energy 2004;76:591–601.

[19] Chow TT. A review on photovoltaic/thermal hybrid solar technology. Appl Energy 2010;87:365–79. doi:10.1016/j.apenergy.2009.06.037.

[20] Redpath DAG, Singh H, Tierney C, Dalzell P. An Experimental Comparison of two Solar Photovoltaic- Thermal (PVT) Energy Conversion Systems for Production of Heat and Power. Energy and Power 2012;2:46–50. doi:10.5923/j.ep.20120204.01.

[21] PVT Roadmap – a European guide for the development and market introduction of PV-thermal technology. PVT Forum 2006. www.pvtforum.org/index.html.

[22] Agarwal RK, Garg HP. Study of a photovoltaic-thermal system—Thermosyphonic solar water heater combined with solar cells. Energy Convers Manag 1994;35:605–20. doi:10.1016/0196-8904(94)90044-2.

[23] Yahya N, Momoh M, Garba M. Design and Construction of a Thermosiphonic Solar Photovoltaic- Thermal Water Heating System. IOSR J Appl Phys 2015;7:88–96. doi:10.9790/4861-07228896.

[24] Chow TT, Pei G, Fong KF, Lin Z, Chan ALS, Ji J. Energy and exergy analysis of photovoltaic-thermal collector with and without glass cover. Appl Energy

2009;86:310–6. doi:10.1016/j.apenergy.2008.04.016.

[25] Allan J, Dehouche Z, Stankovic S, Mauricette L. Performance testing of thermal and photovoltaic thermal solar collectors. Energy Sci Eng 2015;3:310–26. doi:10.1002/ese3.75.

[26] Kim JH, Kim JT. Comparison of electrical and thermal performances of glazed and unglazed PVT collectors. Int J Photoenergy 2012;2012. doi:10.1155/2012/957847.

[27] Sopian K, Yigit KS, Liu HT, Kakaç S, Veziroglu TN. Performance analysis of photovoltaic thermal air heaters. Energy Convers Manag 1996;37:1657–70. doi:10.1016/0196-8904(96)00010-6.

[28] Odeh SD, Abu-mulaweh HI. Design and development of experimental setup of Hybrid PV / Thermal collector. Glob J Eng Educ 2012;14:170–6.

[29] Dorobanțu L, Popescu MO, Popescu CL, Crăciunescu A. Experimental Assessment of PV Panels Front Water Cooling Strategy. Int. Conf. Renew. Energies Power Qual., Bucharest: 2013, p. 1–4.

[30] Zondag HA, de Vries DW, van Helden WGJ, van Zolingen RJC, van Steenhoven AA. The yield of different combined PV-thermal collector designs. Sol Energy 2003;74:253–69. doi:10.1016/S0038-092X(03)00121-X.

[31] Milano P, Aste N, Pero C Del, Leonforte F. Thermal-electrical Optimization of the Configuration a Liquid PVT Collector Thermal-electrical optimization of the configuration a liquid PVT collector. Energy Procedia 2012;30:1–7. doi:10.1016/j.egypro.2012.11.002.

[32] Ibrahim A, Othman MY, Ruslan MH, Alghoul MA, Yahya M, Zaharim A, et al.

Performance of photovoltaic thermal collector (PVT) with different absorbers design. WSEAS Trans Environ Dev 2009;5:321–30.

[33] Al-shamani AN, Mat S, Ruslan MH, Abed AM. Effect of New Ellipse Design on the Performance Enhancement of PV / T Collector : CDF Approach 2016.

[34] Prakash J. Transient analysis of a photovoltaicthermal solar collector for cogeneration of electricity & hot air/water. Energy Convers Manag 1994;35:967–72.

[35] Aste N, Chiesa G, Verri F. Design, development and performance monitoring of a photovoltaic-thermal (PVT) air collector. Renew Energy 2008;33:914–27. doi:10.1016/j.renene.2007.06.022.

[36] Chaji H, Ajabshirchi Y, Esmaeilzadeh E, Heris SZ, Hedayatizadeh M, Kahani M. Experimental study on thermal efficiency of flat plate solar collector using tio2/water nanofluid. Mod Appl Sci 2013;7:60–9. doi:10.5539/mas.v7n10p60.

[37] Ghadimi A, Metselaar IH. The influence of surfactant and ultrasonic processing on improvement of stability, thermal conductivity and viscosity of titania nanofluid. Exp Therm Fluid Sci 2013;51:1–9. doi:10.1016/j.expthermflusci.2013.06.001.

[38] Duangthongsuk W, Wongwises S. An experimental study on the heat transfer performance and pressure drop of TiO2–water nanofluids flowing under a turbulent flow regime. Int J Heat Mass Transf 2010;53:334–44.

[39] Hassani S, Saidur R, Mekhilef S, Hepbasli A. A new correlation for predicting the thermal conductivity of nanofluids; using dimensional analysis. Int J Heat Mass Transf 2015;90:121–30. doi:10.1016/j.ijheatmasstransfer.2015.06.040.

[40] Kim SH, Choi SR, Kim D. Thermal Conductivity of Metal-Oxide Nanofluids:

Particle Size Dependence and Effect of Laser. J Heat Transf 2006;129:298–307. doi:10.1115/1.2427071.

[41] Khanjari Y, Pourfayaz F, Kasaeian AB. Numerical investigation on using of nanofluid in a water-cooled photovoltaic thermal system. Energy Convers Manag 2016;122:263–78. doi:10.1016/j.enconman.2016.05.083.

[42] Nasrin R, Parvin S, Alim MA. Heat transfer by nanofluids through a flat plate solar collector. Procedia Eng 2014;90:364–70. doi:10.1016/j.proeng.2014.11.863.

[43] Sardarabadi M, Passandideh-Fard M. Experimental and numerical study of metal-oxides/water nanofluids as coolant in photovoltaic thermal systems (PVT). Sol Energy Mater Sol Cells 2016;157:533–42. doi:10.1016/j.solmat.2016.07.008.

[44] Taw MM. Experimental studies of nano fl uid thermal conductivity enhancement and applications : A review 2016. doi:10.1016/j.rser.2016.11.111.

[45] Said Z, Sajid MH, Alim MA, Saidur R, Rahim NA. Experimental investigation of the thermophysical properties of AL2O3-nanofluid and its effect on a flat plate solar collector. Int Commun Heat Mass Transf 2013;48:99–107. doi:10.1016/j.icheatmasstransfer.2013.09.005.

[46] Rejeb O, Sardarabadi M, M??n??zo C, Passandideh-Fard M, Dhaou MH, Jemni A. Numerical and model validation of uncovered nanofluid sheet and tube type photovoltaic thermal solar system. Energy Convers Manag 2016;110:367–77. doi:10.1016/j.enconman.2015.11.063.

[47] Sardarabadi M, Passandideh-Fard M, Zeinali Heris S. Experimental investigation of the effects of silica/water nanofluid onPV/T (photovoltaic thermal units). Energy 2014;66:264–72. doi:10.1016/j.energy.2014.01.102.

[48] Verma SK, Tiwari AK, Chauhan DS. Experimental evaluation of flat plate solar collector using nanofluids. Energy Convers Manag 2017;134:103–15. doi:10.1016/j.enconman.2016.12.037.

[49] Parametthanuwat T, Bhuwakietkumjohn N, Rittidech S, Ding Y. Experimental investigation on thermal properties of silver nanofluids. Int J Heat Fluid Flow 2015;56:80–90. doi:10.1016/j.ijheatfluidflow.2015.07.005.

[50] Herrando M, Markides CN. Hybrid PV and solar-thermal systems for domestic heat and power provision in the UK: Techno-economic considerations. Appl Energy 2016;161:512–32. doi:10.1016/j.apenergy.2015.09.025.

[51] Nualboonrueng T. A simulation of the performance of PV-thermal (PVT) systems for residential application in Tokyo. 太陽エネルギー= Sol … 2012;38:37–46.

[52] Rekha L, Vijayalakshmi MM, Natarajan E. Photovoltaic thermal hybrid solar system for residential applications. Energy Sources, Part A Recover Util Environ Eff 2016;38:951–9. doi:10.1080/15567036.2011.651560.

[53] Tripanagnostopoulos Y, Souliotis M, Battisti R, Corrado A. Energy, cost and LCA results of PV and hybrid PV/T solar systems. Prog Photovoltaics Res Appl 2005;13:235–50. doi:10.1002/pip.590.

[54] Kalogirou SA. Use a TRNSYS for modelling and simulation of a hybrid pv-thermal solar system for Cyprus. Renew Energy 2001;23:247–60. doi:10.1016/S0960-1481(00)00176-2.

[55] Tse K-K, Chow T-T, Su Y. Performance evaluation and economic analysis of a full scale water-based photovoltaic/thermal (PV/T) system in an office building. Energy Build 2016;122:42–52. doi:10.1016/j.enbuild.2016.04.014.

[56] Agrawal B, Tiwari GN. Life cycle cost assessment of building integrated photovoltaic thermal (BIPVT) systems. Energy Build 2010;42:1472–81. doi:10.1016/j.enbuild.2010.03.017.

[57] Al-Shamani AN, Sopian K, Mat S, Hasan HA, Abed AM, Ruslan MH. Experimental studies of rectangular tube absorber photovoltaic thermal collector with various types of nanofluids under the tropical climate conditions. Energy Convers Manag 2016;124:528–42. doi:10.1016/j.enconman.2016.07.052.

[58] Kumar V, Afrin S, Ortega J, Sepulveda A, Delgado PM, Aguilar D, et al. Development and evaluation of a prototype concentrating solar collector with thermocline based thermal energy storage for residential thermal usage. J Renew Sustain Energy 2013;5. doi:10.1063/1.4824981.

[59] Bailey JM. Modelling phase change material thermal storage systems n.d.

[60] Muhammad MD, Badr O, Yeung H. CFD Modeling of the Charging and Discharging of a Shell-and-Tube Latent Heat Storage System for High-Temperature Applications. Numer Heat Transf Part a-Applications 2015;68:813–26. doi:10.1080/10407782.2015.1023094.

[61] Gharebaghi M, Sezai I. Enhancement of Heat Transfer in Latent Heat Storage Modules with Internal Fins. Numer Heat Transf Part A Appl 2007;53:749–65. doi:10.1080/10407780701715786.

[62] Yilbas BS, Anwar MK. Design of a mobile thermal battery and analysis of thermal characteristics. J Renew Sustain Energy 2016;8. doi:Artn 02410210.1063/1.4943662.

[63] Taylor RA, Chung C-Y, Morrison K, Hawkes ER. Analysis and Testing of a

Portable Thermal Battery. J Therm Sci Eng Appl 2014;6:31004. doi:10.1115/1.4026092.

[64] Sharma A, Chen C. Solar Water Heating System with Phase Change Materials. Int Rev Chem … 2009;1:297–307.

[65] Malik M, Dincer I, Rosen MA. Review on use of phase change materials in battery thermal management for electric and hybrid electric vehicles. Int J ENERGY Res 2016;40:1011–1031. doi:10.1002/er.3496.

[66] Alaidroos A, He L, Krarti M. Feasibility of Renewable Energy Based Distributed Generations in Yanbu , Saudi Arabia. World Renew Energy Forum 2012:1–8. doi:10.13140/2.1.1132.7049.

[67] Gelažanskas L, Gamage K. Forecasting HotWater Consumption in Residential Houses. Energies 2015;8:12702–17. doi:10.3390/en81112336.

[68] Ghafoor A, Munir A. Design and economics analysis of an off-grid PV system for household electrification. Renew Sustain Energy Rev 2015;42:496–502. doi:10.1016/j.rser.2014.10.012.

[69] Duffie J.A. and BWA. Solar Engineering of Thermal Processes. 3rd ed. New York: John Wiley and Sons; 2006.

[70] Kakaç S, Pramuanjaroenkij A. Review of convective heat transfer enhancement with nanofluids. Int J Heat Mass Transf 2009;52:3187–96. doi:10.1016/j.ijheatmasstransfer.2009.02.006.

[71] Mishra PC, Mukherjee S, Nayak SK, Panda A. A brief review on viscosity of nanofluids. Int Nano Lett 2014;4:109–20. doi:10.1007/s40089-014-0126-3.

[72] O'Hanley H, Buongiorno J, McKrell T, Hu L -w. Measurement and Model

Validation of Nanofluid Specific Heat Capacity with Differential Scanning Calorimetry. Adv Mech Eng 2015;4:181079–181079. doi:10.1155/2012/181079.

[73] Kakaç S, Liu H. Heat Exchangers: Selection, Rating, and Thermal Design. Second. Florida: CRC Press; 2002.

[74] Bhattarai S, Oh JH, Euh SH, Krishna Kafle G, Hyun Kim D. Simulation and model validation of sheet and tube type photovoltaic thermal solar system and conventional solar collecting system in transient states. Sol Energy Mater Sol Cells 2012;103:184–93. doi:10.1016/j.solmat.2012.04.017.

[75] Rossi C, Tagliafico LA, Scarpa F, Bianco V. Experimental and numerical results from hybrid retrofitted photovoltaic panels. Energy Convers Manag 2013;76:634–44. doi:10.1016/j.enconman.2013.07.088.

[76] Amrizal N, Chemisana D, Rosell JI. Hybrid photovoltaic-thermal solar collectors dynamic modeling. Appl Energy 2013;101:797–807. doi:10.1016/j.apenergy.2012.08.020.

[77] Guarracino I, Mellor A, Ekins-Daukes NJ, Markides CN. Dynamic coupled thermal-and-electrical modelling of sheet-and-tube hybrid photovoltaic/thermal (PVT) collectors. Appl Therm Eng 2016;101:778–95. doi:10.1016/j.applthermaleng.2016.02.056.

[78] Baseline Determination for the Electricity Grid in the Kingdom of Saudi Arabia – Grid emission factor (GEF) according to CDM regulations Background. 2010.

Vitae

Name	: Muhammad Owais Lari
Nationality	: Pakistan
Date of Birth	: 01/08/1991
Email	: owais943@gmail.com
Address	: Block C Street # 7 House #5 Nazimabad No.2, Karachi, Pakistan.
Academic Background	: Master of Science (MSc.) Mechanical Engineering (Thermo-fluids), King Fahd University of Petroleum and Minerals, Dhahran, Saudi Arabia. Bachelor of Science in Mechanical Engineering, Pakistan Navy Engineering College, Karachi, Pakistan.
Academic Research	• Junaid Ahmed, I.H. Toor, U.Hayat, M.R.Yousaf, M.O.Lari, "Effect of heat treatment on the electrochemical properties of galvanneal steel in stripping solution", In: 16th Middle East Corrosion Conference and Exhibition, Manama, Bahrain; 2016. (Published)

- Muhammad O. Lari, Ahmet Z.Sahin, "Design, performance and economic analysis of a nanofluid-based photovoltaic/thermal system for residential applications", Energy Conversion and Management 149 (2017) 467-484. (Published)
- Muhammad O. Lari, Ahmet Z.Sahin, "Effect of retrofitting a nanofluid-based photovoltaic/thermal system with a PCM-Thermal battery for residential applications", Renewable Energy (2017). (Submitted)